Ocean Engineering 249 (2022) 110760

Contents lists available at ScienceDirect

Ocean Engineering

journal homepage: www.elsevier.com/locate/oceaneng

Online wave direction and wave number estimation from surface vessel motions using distributed inertial measurement arrays and phase-time-path-differences

Johann A. Dirdal [a,*], Roger Skjetne [b], Jan Roháč [c], Thor I. Fossen [a]

[a] Department of Engineering Cybernetics, Norwegian University of Science and Technology (NTNU), NO-7491, Trondheim, Norway
[b] Department of Marine Technology, Norwegian University of Science and Technology (NTNU), NO-7491, Trondheim, Norway
[c] Dept. of Measurement, Faculty of Electrical Engineering, Czech Technical University in Prague, Prague, Czech Republic

ARTICLE INFO

Keywords:
Kalman filter
Shipboard wave estimation
IMU
Phase-time-path-difference
Marine cybernetics

ABSTRACT

A common approach for finding the direction of ocean waves is to use the phase-time-path-differences (PTPDs) between a static array of various types of sensors mounted on either the sea surface or seabed. However, some practical drawbacks of such arrays are that they tend to be expensive, difficult to install, and fixed in location. We show that the PTPD approach can be generalized to a portable *shipboard* array of spatially distributed sensors rendering it more practical. In this respect, we derive a nonlinear PTPD model for shipboard sensor arrays and prove that the wave direction *and* wave number can be resolved from a minimum of three noncollinear sensors using observability analysis. Moreover, based on our PTPD model, we propose an unscented Kalman filter algorithm for online estimation of the wave direction and wave number, which offers a convenient framework for adding multiple measurements and incorporating uncertainties. Our experimental results from model basin testing with a model ship equipped with several inertial measurement units (IMUs) confirm that the wave direction and wave number can be estimated from the wave-induced motions of a surface vessel with a minimum of three noncollinear IMUs. In this study, we consider parameter estimation for regular waves and assume a dynamically positioned surface vessel with small roll and pitch angles.

1. Introduction

The physical separation distance between two local sensors embedded on the sea surface introduces a delay between the recorded waves passing through them. This delay manifests itself as either a phase, time, or path difference (PTPD) between the wave signals recorded in each sensor. A common technique for finding the direction of ocean waves is to use the PTPDs between the recorded wave signals from several such sensors (e.g., pressure transducers, wave staffs, wave probes, lasers, echo sounders, current meters) mounted on either the sea surface or seabed. This configuration of sensors in the ocean is generally called a wave array, and several works have been reported analyzing the capabilities of such arrays to resolve the wave direction (Esteva, 1976, 1977; Fernandes et al., 1988, 2000; Draycott et al., 2015, 2016, 2018; Luo et al., 2020). However, some important practical drawbacks of wave arrays are that they tend to be expensive, difficult to install, and fixed in location with little flexibility to changes in the design after installation.

Shipboard arrays, on the other hand, are more practical, offering a portable platform that is generally not location restricted and considerably more flexible when it comes to making changes to the installation. Furthermore, shipboard arrays can be used for wave estimation without ship information since the PTPD approach is inherently signal-based (i.e., estimation is done directly from sensor measurements). This useful feature distinguishes the PTPD approach from other signal-based methods using machine learning (Mak and Düz, 2019; Duz et al., 2019), which require ship-specific datasets, thus limiting its generalization to other vessels. The PTPD approach also differs from shipboard model-based methods, which are based on the wave buoy analogy (Waals et al., 2002; Tannuri et al., 2003; Nielsen, 2006; Pascoal and Guedes Soares, 2009; Nielsen, 2017; Brodtkorb et al., 2018) and use sensor measurements together with response amplitude operators (RAOs). RAOs are ship-dependent transfer functions that enable the estimation of the amplitude and direction of waves. However, without ship information, the wave amplitude cannot be estimated in the PTPD

* Corresponding author.
E-mail addresses: johann.a.dirdal@ntnu.no (J.A. Dirdal), roger.skjetne@ntnu.no (R. Skjetne), xrohac@fel.cvut.cz (J. Roháč), thor.fossen@ntnu.no (T.I. Fossen).

https://doi.org/10.1016/j.oceaneng.2022.110760
Received 6 May 2021; Received in revised form 31 January 2022; Accepted 1 February 2022
Available online 25 February 2022

approach with shipboard arrays. Moreover, to our knowledge, only a few studies have considered using a shipboard array of sensors for wave estimation (Fu et al., 2011; Udjus, 2017; Heyn et al., 2017), and these studies only consider the wave direction, although it is theoretically possible to obtain the wave number from the same PTPD data (Donelan et al., 1996; Fernandes et al., 2001).

A prerequisite for the success of both shipboard and standard wave arrays is accurate measurements of the PTPDs. The PTPD is susceptible to several sources of error such as sensor noise, sensor imperfections (e.g., nonlinear sensitivity character and non-orthogonality and misalignment character between the inner sensitive axes), inexact sensor locations and alignment when installed, and, most prominently, the sensor sampling rate. Although some of the literature mentioned above has shown awareness of some of these errors, only a few works have attempted a formal analysis investigating their quantitative impact (Pascal et al., 2009; Pascal and Bryden, 2011). However, those analyzes are mainly restricted to sensor positioning errors with little account taken for the other abovementioned sources. Additionally, despite the prevalence of these errors, there currently does not seem to exist a method indicating the expected uncertainty in the wave estimates.

One of the main goals of the present study is to promote some of the attractive features of inertial measurements units (IMUs) that make them particularly suitable as sensors for shipboard wave arrays. IMUs may add more design flexibility and PTPD accuracy since they are small, lightweight, cheap, easy to install, and have high sampling rates. Despite its attractive features, only a few works have, to our knowledge, considered using shipboard IMU arrays for wave direction estimation (Udjus, 2017; Heyn et al., 2017). In the latter, the authors mount multiple IMUs along the hull of a model-ship and use the PTPD from estimated heave accelerations to determine the direction of incoming harmonic waves. However, it is not clear from the previous study how many IMUs are needed, how far they should be separated, or how they should be arranged to attain reliable estimates of the wave direction.

In this paper, we extend earlier results by the following contributions: First, we derive a nonlinear PTPD model for surface vessels and prove using observability analysis that the wave number can, in addition to the wave direction, also be resolved from a minimum of three noncollinear sensors measuring regular harmonic waves, assuming a dynamically positioned surface vessel with small roll and pitch angles. Second, we propose an unscented Kalman filter (UKF) algorithm for online estimation of the wave direction and wave number. Third, we offer an extended error analysis discussing and quantifying several sources of error associated with shipboard arrays. Some of these errors are then reflected in the error covariance of the UKF, which gives an estimate of the uncertainty to be expected in the computed wave estimates. To our knowledge, we are the first to offer this type of error analysis and propose a method capable of yielding uncertainties in the wave estimates. Fourth, we highlight some important practical considerations regarding the number, separation, and arrangement of sensors from traditional wave arrays that should also be considered when designing shipboard arrays. Finally, the estimation results from several wave tank experiments considering regular waves and a model ship equipped with several IMUs are shown. The results, in general, verify that the wave direction and wave number can be estimated from a minimum of three IMUs.

2. Methodology

It takes time for a wave to travel from one location to another. This travel time induces a phase-time-path-difference (PTPD) between the wave elevation signals recorded at each (sensor) location, which, in turn, can be used to uniquely determine the wave direction and wave number. In this section, we derive a kinematic PTPD model for surface vessels and prove that the relative wave direction and wave number can be resolved uniquely from a minimum of three noncollinear arranged sensors, assuming regular harmonic waves and small roll and pitch angles. The small-angle assumption, which we deem appropriate for roll and pitch angles up to 2°, represents a first step in the research on wave estimation from shipboard sensor arrays utilizing the PTPD concept.

2.1. A phase-time-path-difference model for surface vessels

The PTPD between two signals recorded at two spatially separated locations on a surface vessel can be modeled by considering the distance a wave must travel to get from one sensor to another. The general scenario is depicted in Fig. 1: A dynamically positioned vessel is being struck by long-crested waves that must travel a distance d_{12} in the tangent plane $\{w\}$ to get from sensor $\{s_2\}$ to $\{s_1\}$, which, in turn, creates a delay between the signals in these sensors. The delay, represented by the distance or path difference d_{12}, is time-varying because of the wave-induced vessel roll and pitch motions (the distance between the sensors in the tangent plane $\{w\}$ changes as the vessel begins to tilt due to the wave passing through it; see Fig. 1b) and can be expressed mathematically by transforming the body-fixed position vector $\vec{p}_{s_1s_2}$ to the tangent plane and extracting the x-component of this vector, i.e.,

$$\mathbf{p}^{w}_{s_1s_2} = \mathbf{R}^{w}_{s_1}\mathbf{p}^{s_1}_{s_1s_2}, \tag{1}$$

where $\mathbf{p}^{w}_{s_1s_2}$ is the position of $\{s_2\}$ relative $\{s_1\}$ expressed in $\{w\}$, $\mathbf{p}^{s_1}_{s_1s_2}$ is the coordinate vector of $\{s_2\}$ relative $\{s_1\}$ expressed in $\{s_1\}$, and $\mathbf{R}^{w}_{s_1}$ is a rotation matrix representing a coordinate transformation from $\{s_1\}$ to $\{w\}$. The matrix $\mathbf{R}^{w}_{s_1}$ can be described by a sequence of principal rotations based on the zyx-convention (Fossen, 2021) with angles β, π, θ, and ϕ (Fig. 2). Following this convention, the resulting transform can then be expressed as

$$\mathbf{R}^{w}_{s_1} = \mathbf{R}_{z,\beta}\mathbf{R}_{x,\pi}\mathbf{R}_{y,\theta}\mathbf{R}_{x,\phi} = \begin{bmatrix} c\beta c\theta & c\beta s\theta s\phi + s\beta c\phi & c\beta s\theta c\phi - s\beta s\phi \\ s\beta c\theta & s\beta s\theta s\phi - c\beta c\phi & s\beta s\theta c\phi + c\beta s\phi \\ s\theta & -c\theta s\phi & -c\theta c\phi \end{bmatrix},$$

where $s\,\cdot = \sin(\cdot)$ and $c\,\cdot = \cos(\cdot)$. Using the rotational transform above, an expression for the position vector $\mathbf{p}^{w}_{s_1s_2}$ can be obtained by carrying out the multiplication given by (1), which yields

$$\mathbf{p}^{w}_{s_1s_2} = \begin{bmatrix} R_{12}\left(c\beta c\theta c\alpha_{12} + c\beta s\theta s\phi s\alpha_{12} + s\beta c\phi s\alpha_{12}\right) + z_{12}(c\beta s\theta c\phi - s\beta s\phi) \\ * \\ * \end{bmatrix}, \tag{2}$$

where the body-fixed coordinate vector $\mathbf{p}^{s_1}_{s_1s_2}$ is given in terms of cylindrical coordinates $(R_{12}, \alpha_{12}, z_{12})$ which, respectively, represent the radial distance, angular displacement in the horizontal plane, and sensor height separation of $\{s_2\}$ with respect to $\{s_1\}$. The path difference d_{12} is simply the x-component of (2) and the time it takes the wave to travel from $\{s_2\}$ to $\{s_1\}$ is given by

$$\begin{aligned} t_{12} &= \frac{d_{12}}{c} \\ &= \frac{R_{12}\left(c\beta c\theta c\alpha_{12} + c\beta s\theta s\phi s\alpha_{12} + s\beta c\phi s\alpha_{12}\right) + z_{12}(c\beta s\theta c\phi - s\beta s\phi)}{c}, \end{aligned} \tag{3}$$

where t_{12} represents the time difference between the recorded signals in $\{s_1\}$ and $\{s_2\}$. The wave celerity c (also known as the phase velocity) is given in terms of the wave frequency ω and wave number k by $c = \omega/k$. Using this fact, the time difference (3) can instead be expressed as a phase difference in the case of a harmonic wave, i.e.,

$$\Theta_{12} = kR_{12}\left(c\beta c\theta c\alpha_{12} + c\beta s\theta s\phi s\alpha_{12} + s\beta c\phi s\alpha_{12}\right) + kz_{12}(c\beta s\theta c\phi - s\beta s\phi), \tag{4}$$

where $\Theta_{12} = \omega t_{12}$ is the time-varying phase difference between $\{s_1\}$ and $\{s_2\}$ as a function of k, β, ϕ, and θ. For small ϕ and θ angles (characteristic of large vessels in moderate sea states), (4) reduces to the following expression

$$\Theta_{12} \approx kR_{12}\cos(\beta - \alpha_{12}), \tag{5}$$

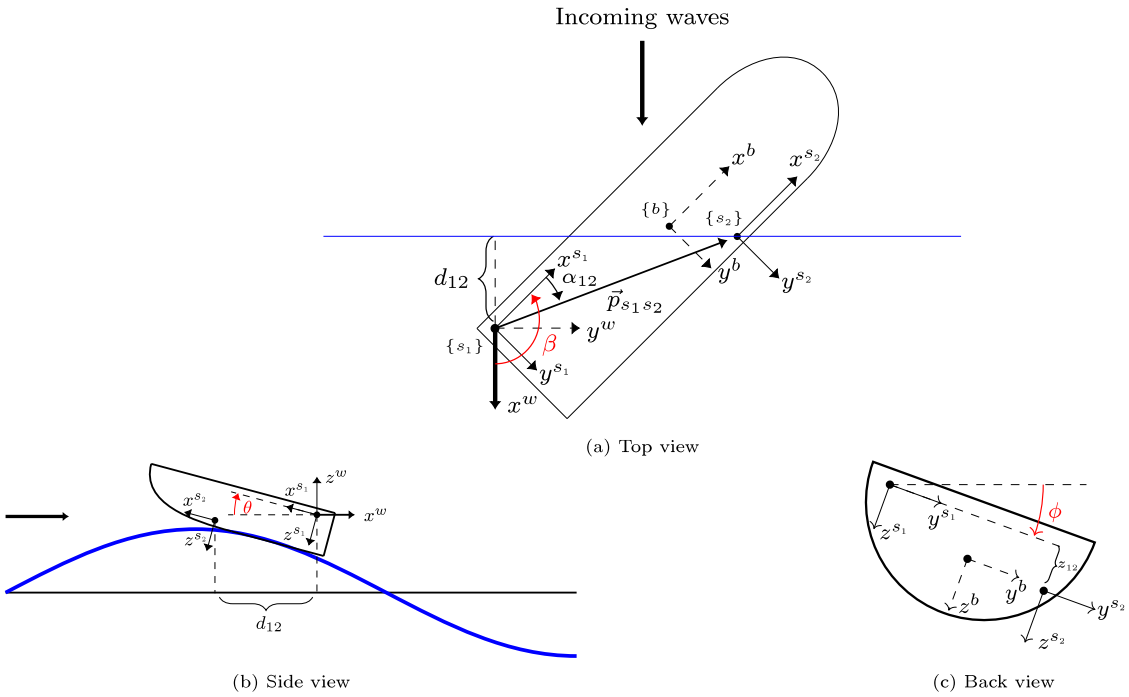

Fig. 1. Snapshots showing three independent situations of a dynamically positioned surface vessel being struck by long-crested waves. The induced rigid body vessel motions are recorded by two spatially distributed sensors denoted $\{s_1\}$ and $\{s_2\}$ with sensor axes $(x^{s_1}, y^{s_1}, z^{s_1})$ and $(x^{s_2}, y^{s_2}, z^{s_2})$ aligned with the body frame $\{b\}$. The position of $\{s_2\}$ relative to $\{s_1\}$ is denoted by the body-fixed vector $\vec{p}_{s_1 s_2}$ and angle α_{12}. The tangent plane $\{w\}$ moves up and down with the vessel and is defined by its x^w, y^w, and z^w axes with the origin coinciding with the chosen reference sensor (here $\{s_1\}$). The x^w axis is defined such that it points in the same direction as the propagating waves, the z^w axis points upwards, and the y^w axis completes the right-handed coordinate system. The distance d_{12} between $\{s_1\}$ and $\{s_2\}$ causes a delay in the recorded signals which depends on the roll (ϕ), pitch (θ), and relative wave direction (β) angles. The relative wave direction β is defined as the counterclockwise angle from x^w to x^{s_1} projected onto the tangent plane $\{w\}$. Starboard incident waves are defined by $\beta \in (-180, 0]°$, whereas port incident waves are defined by $\beta \in (0, 180]°$. When $\beta = 0°$, the waves hit the stern first as the boat heading axis (x^{s_1}) is oriented in the same direction as the waves (x^w).

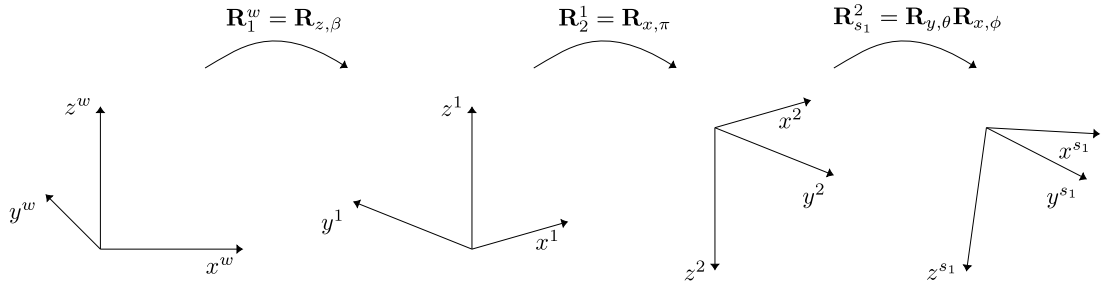

Fig. 2. The rotation matrix from $\{s_1\}$ to $\{w\}$ can be described by a combination of two rotation sequences based on the zyx-convention: A sequence from tangent plane $\{w\}$ to intermediate tangent plane $\{2\}$ (with z-axis pointing downwards) and a sequence from $\{2\}$ to $\{s_1\}$. The principal rotations are given in terms of angles β, π, θ, and ϕ.

which is the standard (constant) phase difference equation commonly found in the literature on wave arrays using the PTPD concept and is the main research focus of this article. Several experiments were performed verifying the correctness of the small-angle assumption. In all experiments considered, the vessel roll and pitch angles were within the range ±2° (Section 5.2), and the height separation between the lowest and highest sensor was measured to be around 16 cm. Together, these values justify the transition from (4) to (5), and our experimental results (Section 5.5.1) also confirm that the small-angle model worked well for those values. However, it is presently unclear how far the roll and pitch angles can be extended before the small-angle assumption is violated.

2.2. Analytical solution

For small roll and pitch angles, an analytical solution of the wave direction can be found by adding an additional sensor $\{s_3\}$ to the surface vessel in Fig. 1, which yields an additional phase difference measurement, i.e.,

$$\Theta_{13} \approx k R_{13} \cos(\beta - \alpha_{13}). \tag{6}$$

Expanding (5) and (6), and grouping the measurements into a 2×1 matrix, yields the system

$$\begin{bmatrix} \Theta_{12} \\ \Theta_{13} \end{bmatrix} = k \begin{bmatrix} R_{12}\cos\alpha_{12} & R_{12}\sin\alpha_{12} \\ R_{13}\cos\alpha_{13} & R_{13}\sin\alpha_{13} \end{bmatrix} \begin{bmatrix} \cos\beta \\ \sin\beta \end{bmatrix}.$$

The wave direction can be isolated by applying the 2×2 inverse to the right-hand side above, thus leaving us with

$$\begin{bmatrix} \cos\beta \\ \sin\beta \end{bmatrix} = \frac{1}{k R_{12} R_{13} \sin(\alpha_{13} - \alpha_{12})} \begin{bmatrix} (R_{13}\sin\alpha_{13})\Theta_{12} - (R_{12}\sin\alpha_{12})\Theta_{13} \\ (R_{12}\cos\alpha_{12})\Theta_{13} - (R_{13}\cos\alpha_{13})\Theta_{12} \end{bmatrix}.$$

Hence, the analytical expression of the wave direction becomes

$$\beta = \arctan\left(\frac{[(R_{12}\cos\alpha_{12})\Theta_{13} - (R_{13}\cos\alpha_{13})\Theta_{12}]/\mathrm{sgn}(D)}{[(R_{13}\sin\alpha_{13})\Theta_{12} - (R_{12}\sin\alpha_{12})\Theta_{13}]/\mathrm{sgn}(D)} \right). \tag{7}$$

where

$$D = kR_{12}R_{13}\sin(\alpha_{13} - \alpha_{12}). \tag{8}$$

The above analysis shows that the wave direction can be uniquely determined from (7) provided that (i) a minimum of three sensors are used, and (ii) they are arranged in a noncollinear configuration on the vessel—thus ensuring that (8) is non-zero.

Eq. (7) is arguably the de facto standard for computing the mean wave direction with arrays (Esteva, 1976, 1977; Fernandes et al., 1988, 2000; Draycott et al., 2015, 2016, 2018; Luo et al., 2020). However, this approach has some important drawbacks that render it unsuitable for applications requiring real-time or online estimates of the wave direction. In particular, the analytical solution (7) neither provides a measure of uncertainty in the wave direction estimates (despite the phase difference and sensor locations being subject to error) nor an estimate of the wave number, although, as we shall see, can be obtained from the same set of measurements. Also, the analytical solution does not offer a convenient framework for adding additional measurements. The Kalman filter framework will alleviate all these issues.

2.3. Kalman filter state–space model

Let R_{ij} and α_{ij} be the polar coordinates of sensor $\{s_j\}$ (slave) relative to sensor $\{s_i\}$, where $\{s_i\}$ is taken to be the chosen master/reference sensor. Using this notation, (5) and (6) can be expressed more generally as

$$\Theta_{ij} = kR_{ij}\cos(\beta - \alpha_{ij}), \tag{9}$$

where Θ_{ij} represents the phase difference between the heave signals recorded by sensors $\{s_i\}$ and $\{s_j\}$. Expanding (9) and introducing the state vector $\mathbf{x} = [x_1,\ x_2]^\top = [\beta,\ k]^\top$, the expression can be reformulated into

$$\Theta_{ij} = \begin{bmatrix} R_{ij}\cos\alpha_{ij} & R_{ij}\sin\alpha_{ij} \end{bmatrix} \begin{bmatrix} x_2\cos x_1 \\ x_2\sin x_1 \end{bmatrix}.$$

For $N \geq 3$ (number of sensors), the final Kalman filter state–space model becomes

$$\dot{\mathbf{x}} = \mathbf{0},$$
$$\mathbf{z} = \mathbf{h}(\mathbf{x}) = \underbrace{\begin{bmatrix} R_{12}\cos\alpha_{12} & R_{12}\sin\alpha_{12} \\ R_{13}\cos\alpha_{13} & R_{13}\sin\alpha_{13} \\ \vdots & \vdots \\ R_{1N}\cos\alpha_{1N} & R_{1N}\sin\alpha_{1N} \\ R_{23}\cos\alpha_{23} & R_{23}\sin\alpha_{23} \\ \vdots & \vdots \\ R_{2N}\cos\alpha_{2N} & R_{2N}\sin\alpha_{2N} \\ \vdots & \vdots \\ R_{(N-1)N}\cos\alpha_{(N-1)N} & R_{(N-1)N}\sin\alpha_{(N-1)N} \end{bmatrix}}_{\text{configuration matrix}} \begin{bmatrix} x_2\cos x_1 \\ x_2\sin x_1 \end{bmatrix}, \tag{10}$$

where $\mathbf{z} = [\Theta_{12},\ \Theta_{13}, \ldots,\ \Theta_{1N},\ \Theta_{23},\ \ldots, \Theta_{2N},\ \ldots, \Theta_{(N-1)N}]^\top$. The dimension of $\mathbf{z}$ is given by the maximum number of distinct phase difference measurements associated with N, which can be calculated using (23).

2.4. Observability results

It was shown in Section 2.2 that a minimum of three noncollinear arranged sensors is needed to determine the wave direction uniquely. The analysis, however, does not show that the wave number may also be resolved from the same set of measurements, which—based on the reported literature (Donelan et al., 1996; Fernandes et al., 2001)—seems to be a less known fact. This interesting fact can be proved by showing that the state–space model in (10) is observable for a minimum of two distinct PTPD measurements (three noncollinear sensors). The results from the observability analysis (see Appendix A) are summarized in the following theorem:

Theorem 1 (*Minimum Sensor Configuration*). *Consider a single harmonic wave with wave number k and relative wave direction β (Fig. 1), then k and β can be uniquely determined from a dynamically positioned surface vessel with small roll and pitch angles using a minimum of three noncollinear spatially distributed sensors measuring the vessel's heave motion.*

Proof. See Appendix A.

3. Estimation algorithm and error analysis

The PTPD state–space model (10) is by nature nonlinear, indicating that nonlinear estimation techniques should be considered to find the wave direction and wave number. It is worth emphasizing that the wave number should be positive, which introduces a constraint on the state estimate. In this section, we look at two different methods for achieving the above goals, namely, the extended Kalman filter (EKF) and unscented Kalman filter (UKF) algorithms (Brown and Hwang, 1997; Julier and Uhlmann, 2004). Although the EKF is more renowned and conceptually easier to grasp, the UKF has advantages for highly nonlinear systems containing state constraints.

3.1. Extended vs. unscented Kalman filter

When a state–space representation contains nonlinearities in either the process model, measurement model, or both, the EKF algorithm has proven to be a viable option, capable of providing reliable state estimates for a wide range of applications. However, despite its success, the EKF suffers from some serious limitations.

In short, the EKF algorithm linearizes all nonlinear transformations related to the noise covariance progressions and inserts them in place of the linear transformations of a regular Kalman filter. While this estimation strategy has proven successful for many systems, in particular those whose dynamics can be considered almost linear, the EKF has not demonstrated the same level of success for highly nonlinear systems (Julier and Uhlmann, 2004). The reason for this is mainly due to its inherent use of linearization, which loses accuracy as the transformations become increasingly nonlinear.

When constraints are imposed on states, the state estimates from an EKF do not always converge to the true values (Kandepu et al., 2008). The standard way of handling constraints in the EKF is known as "clipping" (Haseltine and Rawlings, 2005), which involves projecting the estimates onto the boundary of the feasible region whenever they are outside it. The drawback of this strategy is that the constraint information has no effect on the covariances of the EKF estimates.

The UKF overcomes the aforementioned limitations by eliminating the need for linearization altogether, while simultaneously updating the covariances to account for constraints. In short, the UKF samples a fixed number of points around the mean (called *sigma* points) and propagates these points through the associated nonlinear transforms to obtain new sample points—from which new estimates of the mean and covariance are obtained. If the sampled points are outside the feasible region, they are projected onto the boundary, similar to "clipping", except that the updated covariance is based on these points instead.

3.2. UKF algorithm

The UKF may be applied to systems of the form

$$\begin{aligned} \mathbf{x}_{k+1} &= \mathbf{f}(\mathbf{x}_k) + \mathbf{w}_k, \quad \mathbf{w}_k \sim \mathcal{N}(\mathbf{0},\ \mathbf{Q}_k), \\ \mathbf{z}_k &= \mathbf{h}(\mathbf{x}_k) + \mathbf{v}_k, \quad \mathbf{v}_k \sim \mathcal{N}(\mathbf{0},\ \mathbf{R}_k), \end{aligned} \tag{11}$$

where $\mathbf{f}$ and $\mathbf{h}$ represent nonlinear vector fields, $\mathbf{x}_k := \mathbf{x}(kT_s)$ and $\mathbf{z}_k := \mathbf{z}(kT_s)$ constitute the sampled state and measurement vectors

with T_s and k being the respective sampling time and number (not to be confused with the wave number), and $\mathbf{w}_k$ and $\mathbf{v}_k$ represent white Gaussian process and measurement noise with covariance $\mathbf{Q}_k$ and $\mathbf{R}_k$, respectively. Discretizing (10) and comparing it with (11) shows that the former fits the required model form, with $\mathbf{f}(\mathbf{x}_k) = \mathbf{x}_k$ and $\mathbf{v}_k$ and $\mathbf{w}_k$ discussed in Sections 3.3 and 3.4.

Our UKF wave estimation algorithm is outlined in Algorithm 1; for relevant background material on the UKF and constraint handling, we refer to Brown and Hwang (1997), Julier and Uhlmann (2004), Kandepu et al. (2008) and Simon (2010) and references therein.

The UKF uses a deterministic sampling scheme to select its sample or sigma points, as it is commonly called. In this paper, we have chosen the following set of sigma points

$$X_k^{(i)} = \begin{cases} \hat{\mathbf{x}}_k^-, & i = 0 \\ \hat{\mathbf{x}}_k^- + \sqrt{(L+\lambda)\hat{\mathbf{P}}_k^-}, & i = 1, \dots, L \\ \hat{\mathbf{x}}_k^- - \sqrt{(L+\lambda)\hat{\mathbf{P}}_k^-}, & i = L+1, \dots, 2L \end{cases} \tag{12}$$

where

$\lambda = \alpha^2(L+\kappa) - L$

L = dimension of state $\mathbf{x}_k$

α = spread of samples about the mean

κ = scaling factor

If the sigma points are outside the feasible region, they are projected onto the boundary using the projection

$$P(\hat{x}_2) = \begin{cases} \epsilon, & \hat{x}_2 < \epsilon \\ \hat{x}_2, & \text{otherwise} \end{cases} \tag{13}$$

where $\hat{x}_2$ is the wave number estimate and ϵ is a small positive number representing the boundary of the feasible region. The sigma points are then propagated through the nonlinear transform (10) to yield a new cloud of transformed points. The statistics of these points are then computed by weighting them together using the following sets of weights

$$W_\mu^{(0)} = \frac{\lambda}{\lambda + L}, \; W_\mu^{(0<i\leq 2N)} = \frac{1}{2(\lambda + L)}, \tag{14}$$

$$W_\sigma^{(0)} = W_\mu^{(0)} + 1 - \alpha^2 + \gamma, \; W_\sigma^{(0<i\leq 2L)} = \frac{1}{2(\lambda + L)}. \tag{15}$$

Algorithm 1 Wave algorithm

procedure UKF($\hat{\mathbf{x}}_k^-, \hat{\mathbf{P}}_k^-, \mathbf{z}_k$)

$X_k^{(i)} \leftarrow \text{Sigma}(\hat{\mathbf{x}}_k^-, \hat{\mathbf{P}}_k^-)$ ▷ Compute sigma points using (12)

$X_c^{(i)} \leftarrow P(X_k^{(i)})$ ▷ Project sigma points using (13)

$\hat{\mathbf{x}}_k^- \leftarrow \sum_{i=0}^{2L} W_\mu^{(i)} X_c^{(i)}$ ▷ Compute the apriori state estimate with (14)

$\hat{\mathbf{P}}_k^- \leftarrow \{\sum_{i=0}^{2L} W_\sigma^{(i)} (X_c^{(i)} - \hat{\mathbf{x}}_k^-)(X_c^{(i)} - \hat{\mathbf{x}}_k^-)^\top\} + \mathbf{Q}_k$ ▷ Compute the apriori error covariance with (15)

$Z_k^{(i)} \leftarrow \mathbf{h}(X_c^{(i)})$ ▷ Propagation of sigma points using (10)

$\hat{\mathbf{z}}_k^- \leftarrow \sum_{i=0}^{2L} W_\mu^{(i)} Z_k^{(i)}$ ▷ Predicted measurement

$\hat{\mathbf{S}}_k \leftarrow \{\sum_{i=0}^{2L} W_\sigma^{(i)} (Z_k^{(i)} - \hat{\mathbf{z}}_k^-)(Z_k^{(i)} - \hat{\mathbf{z}}_k^-)^\top\} + \mathbf{R}_k$ ▷ Compute the innovation covariance

$\hat{\mathbf{P}}_k^{\mathbf{xz}} \leftarrow \sum_{i=0}^{2L} W_\sigma^{(i)} (X_c^{(i)} - \hat{\mathbf{x}}_k^-)(Z_k^{(i)} - \hat{\mathbf{z}}_k^-)^\top$ ▷ Compute the cross-covariance

$\mathbf{K}_k \leftarrow \hat{\mathbf{P}}_k^{\mathbf{xz}} \hat{\mathbf{S}}_k^{-1}$ ▷ Compute the Kalman gain

$\hat{\mathbf{x}}_k \leftarrow \hat{\mathbf{x}}_k^- + \mathbf{K}_k(\mathbf{z}_k - \hat{\mathbf{z}}_k^-)$ ▷ Compute posterior state estimate

$\hat{\mathbf{P}}_k \leftarrow \hat{\mathbf{P}}_k^- - \mathbf{K}_k \hat{\mathbf{S}}_k \mathbf{K}_k^\top$ ▷ Compute posterior error covariance

return $\hat{\mathbf{x}}_k, \hat{\mathbf{P}}_k$

end procedure

3.3. Error analysis

Several sources of error are associated with shipboard arrays that may inhibit high-quality wave estimates from the UKF. The errors can generally be grouped as (a) errors caused by sensor imperfections and oscillatory and/or transient effects on the sensors due to structural vibrations (e.g., from the engine) and external environmental conditions, and (b) errors caused by the array construction (e.g., inexact sensor locations and alignment). These errors ultimately affect the obtained phase differences, which, in turn, are used to estimate the wave direction and wave number. It is, therefore, essential to either remove these errors or quantify the uncertainties caused by them so that we may confidently decide whether or not to rely on the wave estimates. In Sections 3.3.1 and 3.3.2 we quantify and discuss strategies for removing the errors caused by (a) and (b), respectively.

3.3.1. Sensor errors

The noise $\mathbf{v}_k$ in (11) reflects the uncertainty associated with the measurement $\mathbf{z}_k$, which, in this case, is the measured phase difference Θ_{ij}. The error in Θ_{ij} can be linked to three primary sources: (i) high-frequency sensor noise and oscillatory and transient effects caused by structural vibrations and/or external environmental conditions, (ii) deterministic sensor imperfections such as axis misalignment, nonlinear sensitivity character, and stochastic bias behavior, and (iii) insufficient sensor sampling rate. Although temporal aliasing due to (iii) may also be a concern, the effect is usually minimized by the high inner sampling rates (typically ≥ 1 kHz) employed in today's IMU technology.

The high-frequency noise content related to (i) may be alleviated by applying a digital lowpass filter, which attenuates noise residing outside the predefined passband (in this application, the cut-off frequency was selected above the maximal wave frequency).

The effects of (ii) will generally manifest themselves as a bias in the specific force measurements of the accelerometers, further impacting the computed phase difference. One possible strategy to resolve the axis misalignment offset is to compare the measured specific force with the gravitational vector during some time when the average linear acceleration of the vessel is known to be zero, and the vessel is assumed to be well balanced (i.e., $\phi = \theta = 0$). This approach will work when the sensor biases can be considered negligible. Assuming that the above assumptions hold, the angle offset in roll and pitch between the sensor and body frames can then be estimated through

$$\delta\phi \approx \arctan\left(\frac{f_y}{f_z}\right), \quad \delta\theta \approx \arctan\left(\frac{f_x}{\sqrt{f_y^2 + f_z^2}}\right),$$

where $\delta\phi$ and $\delta\theta$ are the respective roll and pitch offset angles, and (f_x, f_y, f_z) denote the specific force measurements from the accelerometers (Fossen, 2021). The heading angle offset can, in general, not be determined from accelerometers alone, but may be estimated from a magnetometer. The error related to the nonlinear sensitivity behavior is deemed minimal due to the high-quality sensor technology being employed.

The error from (iii) can be quantified by examining in detail how the phase difference is defined and how it is actually measured. The phase difference between $\{s_i\}$ (master) and $\{s_j\}$ (slave) is defined through the relationship

$$\Theta_{ij} = \omega t_{ij}, \tag{16}$$

where ω is the frequency of the wave and t_{ij} is the time difference (i.e., the time it takes the wave to travel from $\{s_j\}$ to $\{s_i\}$). The time difference is estimated by measuring the lag (number of samples) D_{ij}

between the recorded signals and multiplying it by the sampling time T_s, i.e., $\hat{t}_{ij} = T_s D_{ij}$. Assuming that the effects from (i) and (ii) are handled and do not affect D_{ij}, the error resulting from the sampling time T_s can be bounded by

$$|t_{ij} - \hat{t}_{ij}| \leq t_{\max} := \frac{T_s(D_{ij}+1) - T_s D_{ij}}{2} = \frac{T_s}{2}.$$

The division by two is a property of the algorithm[1] we use to obtain D_{ij}. If we assume further that ω is known precisely, then the maximum phase error due to T_s can be quantified as

$$|\Theta_{ij} - \hat{\Theta}_{ij}| \leq \Theta_{\max} := \frac{\omega T_s}{2}. \tag{17}$$

The phase difference error bound to (17) implies that the *true* phase difference can be located within the interval $[-\omega T_s/2, \omega T_s/2]$ of the corresponding phase estimate. Based on this knowledge, it is possible to use a uniform distribution to model the worst-case phase difference error. However, when the error character can be considered rather similar to jitter, a Gaussian distribution is more appropriate over that specific interval and can be adopted with the same variance as the uniform distribution. The variance is computed as

$$\sigma^2_{\Theta_{\max}} = \frac{1}{12}\left(\frac{\omega T_s}{2} - \left(-\frac{\omega T_s}{2}\right)\right)^2 = \frac{1}{12}\omega^2 T_s^2, \tag{18}$$

and, hence, the measurement covariance $\mathbf{R}_k$ can finally be quantified as

$$\mathbf{R}_k = \sigma^2_{\Theta_{\max}} I_P,$$

where I_P is a $P \times P$ identity matrix with P denoting the number of distinct phase difference measurements.

3.3.2. Sensor positioning errors

In general, the exact position of each shipboard sensor will be subject to uncertainty. We can analyze how this uncertainty influences the predicted phase difference (9) by carrying out the analysis in Section 2.1 again, but with errors associated with each sensor location.

Consider again the vessel in Fig. 1 and let (x_{12}, y_{12}, z_{12}) denote the *exact* coordinate location of sensor $\{s_2\}$ (slave) with respect to sensor $\{s_1\}$ (reference/master), which forms the origin of the local frame with axes perfectly aligned with the vessel body frame. Further, if we define $(\hat{x}_{12}, \hat{y}_{12}, \hat{z}_{12})$ to be the corresponding *estimated* sensor location, then the coordinates of $\{s_2\}$ with respect to $\{s_1\}$ can be written as

$$x_{12} = \hat{x}_{12} + \epsilon_x, \quad y_{12} = \hat{y}_{12} + \epsilon_y, \quad z_{12} = \hat{z}_{12} + \epsilon_z,$$

where we have introduced Gaussian distributed errors ϵ_x, ϵ_y, ϵ_z with zero mean and variance σ^2 (representative of uncertainties of Type A, whereas Type B is considered negligible). The relationships above can be expressed more compactly using vector notation, i.e.,

$$\mathbf{p}^{s_1}_{s_1 s_2} = \begin{bmatrix} x_{12} \\ y_{12} \\ z_{12} \end{bmatrix} = \begin{bmatrix} \hat{x}_{12} \\ \hat{y}_{12} \\ \hat{z}_{12} \end{bmatrix} + \begin{bmatrix} \epsilon_x \\ \epsilon_y \\ \epsilon_z \end{bmatrix}.$$

Following the exact same derivation as in Section 2.1, the (time-varying) phase difference equation between $\{s_1\}$ and $\{s_2\}$ with location uncertainty becomes

$$\begin{aligned}\Theta_{12} = k\big(&\hat{x}_{12}c\beta c\theta + \hat{y}_{12}(c\beta s\theta s\phi + s\beta s\phi)\big) + k\hat{z}_{12}(c\beta s\theta c\phi - s\beta s\phi) \\ &+k\big(\epsilon_x c\beta c\theta + \epsilon_y(c\beta s\theta s\phi + s\beta s\phi)\big) + k\epsilon_z(c\beta s\theta c\phi - s\beta s\phi),\end{aligned}$$

and assuming small roll and pitch angles (i.e., $\phi \approx 0$ and $\theta \approx 0$), the expression above reduces to

$$\Theta_{12} \approx k(\hat{x}_{12}\cos\beta + \hat{y}_{12}\sin\beta) + k(\epsilon_x \cos\beta + \epsilon_y \sin\beta).$$

[1] For more details see: https://se.mathworks.com/help/signal/ref/finddelay.html.

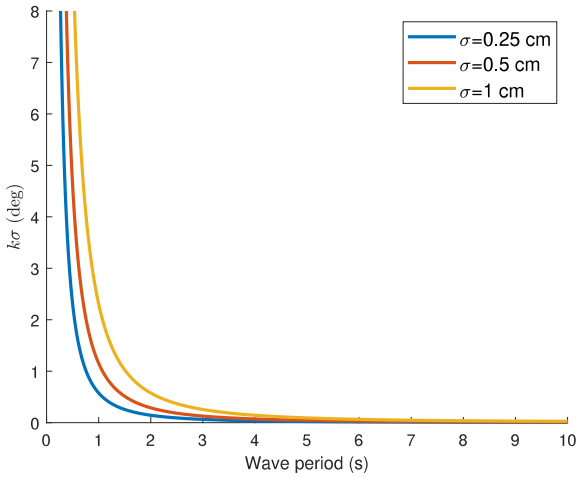

Fig. 3. Bias standard deviation of (20) vs. wave period for various σ. The wave number k is computed for the displayed wave periods using the dispersion relation (21) with constant water depth, $d = 1.5$ m. The results are almost identical for larger water depths.

If we let $\hat{\Theta}_{12} = k(\hat{x}_{12}\cos\beta + \hat{y}_{12}\sin\beta)$ be the estimated phase difference, then the phase error can be written as

$$\Theta_{12} - \hat{\Theta}_{12} \approx k(\epsilon_x \cos\beta + \epsilon_y \sin\beta). \tag{19}$$

From (19), it is clear that the location uncertainty of each sensor manifests itself as a constant bias in the estimated phase difference. In the following, we determine the noise characteristics (i.e., mean and variance) of (19) to have a better understanding of its impact on wave estimation.

If we let $b(k,\beta) = k(\epsilon_x \cos\beta + \epsilon_y \sin\beta)$ denote the state-dependent constant bias, then, when calibrated and compensated, the mean can be considered as

$$\begin{aligned}\mathbb{E}[b(k,\beta)] &= \mathbb{E}[k(\epsilon_x \cos\beta + \epsilon_y \sin\beta)] \\ &= k\cos\beta\mathbb{E}[\epsilon_x] + k\sin\beta\mathbb{E}[\epsilon_y] \\ &= 0,\end{aligned}$$

where we have utilized the Gaussian zero-mean assumption of the sensor positioning errors. Doing the same for the variance, yields

$$\begin{aligned}\mathbb{E}[b(k,\beta)^2] &= \mathbb{E}[k^2(\epsilon_x \cos\beta + \epsilon_y \sin\beta)^2] \\ &= k^2\Big(\cos^2\beta\mathbb{E}[\epsilon_x^2] + 2\sin\beta\cos\beta\mathbb{E}[\epsilon_x\epsilon_y] + \sin^2\beta\mathbb{E}[\epsilon_y^2]\Big) \\ &= k^2\sigma^2,\end{aligned}$$

where we have utilized that ϵ_x and ϵ_y are independent random variables. The noise characteristics above can be generalized to P measurements (assuming the same mean and covariance of the location error for each sensor pair), yielding the mean and covariance information

$$\begin{aligned}\mathbb{E}[\mathbf{b}(k,\beta)] &= \mathbf{0}_{P\times 1} \\ \mathbb{E}[\mathbf{b}(k,\beta)\mathbf{b}(k,\beta)^\top] &= k^2\sigma^2 I_P,\end{aligned} \tag{20}$$

where $\mathbf{b}(k,\beta) = [b_1(k,\beta), b_2(k,\beta), \ldots, b_P(k,\beta)]^\top$, $b_i(k,\beta) = k(\epsilon_{x_i}\cos\beta + \epsilon_{y_i}\sin\beta)$, ϵ_{x_i} and $\epsilon_{y_i} \sim \mathcal{N}(0,\sigma^2)$, and I_P is a $P \times P$ identity matrix.

The bias impact on wave estimation can be seen in Fig. 3, which shows that the standard deviation of the bias is inversely proportional to the wave period. This result suggests that, for sufficiently long wave periods (small frequencies), the biases may be neglected from analysis without incurring substantial errors in the phase difference estimates.

It is worth mentioning that the bias is, in general, not observable as each new sensor introduces another location error and, consequently, a new bias. This can be verified by augmenting the state–space

Table 1
A summary of the initial state estimates, covariances, and internal parameters used in the UKF.

UKF initialization	$\hat{\mathbf{x}}_0^- = [0,\ 0.05]^\top$ $\hat{\mathbf{P}}_0^- = \mathrm{diag}([\frac{\pi^2}{3},\ 2])$
Process and measurement covariance	$\mathbf{Q}_k = \mathbf{0}_{2\times 2}$ $\mathbf{R}_k = \left(\frac{1}{12}\omega^2 T_s^2 + k^2\sigma^2\right) I_P$
UKF parameters	$L = 2, \quad \alpha = 0.01, \quad \gamma = 2, \quad \kappa = 0$

model in (10) to include the bias as an unknown state and checking observability.

3.4. Summary

A summary of the initialization, covariance matrices, and internal parameters used in our UKF algorithm can be found in Table 1. It is worth stressing that faster convergence may be achieved by initializing the wave number to the value given by the dispersion relation, i.e.,

$$\omega^2 = kg\tanh(kd), \tag{21}$$

where g is the gravitational constant and d is the water depth. In this paper, however, we chose the initial values in Table 1 to demonstrate the validity of Theorem 1.

The initial estimated error covariance $\hat{\mathbf{P}}_0^-$ was selected by modeling the initial wave direction error as a uniform distribution over the interval $(-\pi, \pi]$ and approximating it by a Gaussian distribution with the same variance. The wave number variance was chosen heuristically but relatively large, reflecting our uncertainty in the actual value.

The process covariance $\mathbf{Q}_k$ was considered zero due to the states in the process model (10) and conditions of the experiments performed being (more or less) constant. However, this value is not universal as $\mathbf{Q}_k$ should, in general, be adapted to reflect any discrepancy between the state model and the properties of the sea environment being considered. The measurement covariance $\mathbf{R}_k$ was chosen based on our analysis in Section 3.3.1.

4. Shipboard wave array design

In this section, we highlight some important practical considerations when designing shipboard wave arrays. As we shall see, care must be exercised when selecting (a) the separation distance between each sensor, (b) the geometry of the sensor array, (c) sensor type, and (d) number of sensors. All these features ultimately contribute towards our desired end goal—the attainment of accurate estimates of the wave direction and wave number.

To facilitate analysis, we consider two different types of sensor arrays (Fig. 4). These arrays will aid us in demonstrating the key issues with some of the features mentioned above.

4.1. Barber and Doyle criterion

As pointed out by Fernandes et al. (1988, 2000), the criterion of Barber and Doyle (1956) plays a crucial role in the design and construction of wave arrays. The criterion states that the separation distance D between two wave sensors should not exceed half the wavelength λ of the wave passing through them, i.e.,

$$D < \lambda/2, \tag{22}$$

in order for the phase difference between these sensors to be resolved unambiguously. In other words, as long as (22) is satisfied, the theoretical phase difference between the sensors will be restricted to the interval $(-\pi, \pi)$, thus correctly representing the physical situation. The maximum sensor separation imposed by (22) ultimately implies that the wave direction and number cannot be resolved for a range of frequencies (Fig. 5). It is thus important to have an idea of the frequency range of the expected waves and design the separation distances accordingly using (22). For wind-generated surface gravity waves, the wave periods generally range between 0.25 and 30 s.

4.1.1. Case study

The problems associated with (22) are illustrated by considering the polygonal array in Fig. 4a and choosing a wave period for which we want to resolve the wave direction and number. If we select $T = 1.0$ s and $D = 1.33$ m as our desired wave period and separation distance, it can be seen that some of the phase differences associated with this frequency become ambiguous for certain choices of reference sensor (Fig. 6). When selecting sensor 1 as reference, the separation distance to sensor 2 and 4 exceeds the limit imposed by $T = 1.0$ s (i.e., $R_{12} = R_{14} = D = 1.33 > 0.7806$ m), whereas when sensor 3 is chosen as reference, all separation distances ($R_{31} = R_{32} = R_{34} = D' = 0.768 < 0.7806$ m) are within the boundary. Hence, if sensor 1 is naively chosen as a reference, a range of wave directions cannot be resolved no matter how the sensor pairs are selected. It is, however, worth emphasizing that the latter is valid in relation to the imposed period $T = 1.0$ s. There will always be a range of periods (and, consequently, wave directions) that cannot be resolved based on the sensor configuration (Fig. 5), which implies that the wave period(s) should also be considered a design criterion of the system.

4.2. Errors due to sampling rate and sensor location

Unfortunately, the satisfaction of (22) alone is no guarantee to avoid ambiguity in the computed phase difference. As we saw earlier in Section 3.3, the sensor sampling rate and location error will induce errors in the phase difference, which may cause it to exceed the interval $(-\pi, \pi)$—especially if the separation distance is close to the limit given by (22). The situation can be simulated by considering the case study in Section 4.1.1 and adding random Gaussian noise with variances given by (18) and (20) to the theoretical phase difference (9). The simulation results (Fig. 7) confirm that errors from the sampling rate and sensor locations can potentially "push" the phase difference outside the desired range, making it increasingly challenging to resolve the true wave direction and wave number. Therefore, one should consider using sensors with a sufficiently high sampling rate (e.g., IMUs) and ensure that their positioning is known accurately as possible when designing shipboard arrays. A high sampling rate (e.g., 1 kHz) will also reduce the amount of temporal aliasing.

4.3. Multiple measurements

We emphasize that although the wave direction and wave number can be resolved from a minimum of three noncollinear sensors, this number only represents a theoretical lower bound for harmonic waves and does not, in general, reflect optimality. It is, therefore, interesting to study how additional sensors and measurements may impact wave estimation.

Consider the polygonal array in Fig. 4a with $D = 1.33$ m again. The array consists of four sensors yielding a total of six distinct phase difference measurements, as calculated by

$$P_{\max}(N) = \frac{N(N-1)}{2}, \tag{23}$$

where N is the number of sensors and $P_{\max}(N)$ is the maximum number of distinct phase difference measurements associated with N (assuming nonlinear arrays). The phase measurements are generated using (9) for multiple wave directions, and Gaussian random noise with variances given by (18) and (20) is added to simulate the uncertainties caused by the sensor sampling rate and location errors (see Sections 3.3.1 and 3.3.2). By applying the UKF algorithm (Algorithm 1) to this data and inspecting the resulting error covariance $\hat{\mathbf{P}}_k$, it is possible to see

(a) Polygonal array (b) Linear array

Fig. 4. An illustration of the different sensor arrays considered in the analysis of Section 4. The sensors $\{1, 2, 4\}$ in (a) form an equilateral triangle on the horizontal plane with length D and a circumscribed circle at $\{3\}$ with radius $D' = D/\sqrt{3}$.

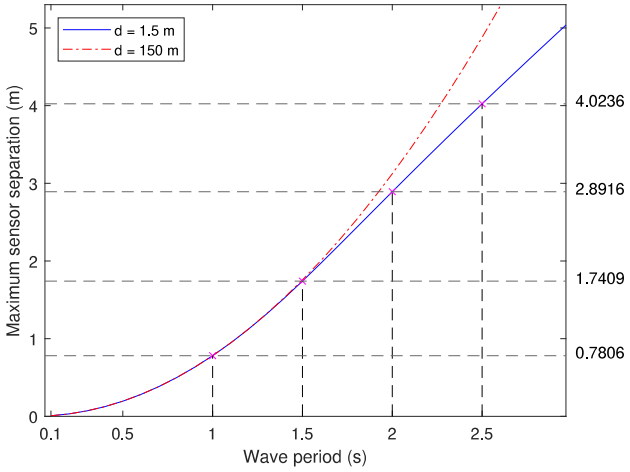

Fig. 5. Maximum sensor separation vs. wave period for water depths $d = 1.5$ and $d = 150$ m. The wave number $k = 2\pi/\lambda$ has been substituted into (22) and plotted against a range of wave periods using (21). The maximum separation distances for which the phase difference can be resolved unambiguously are indicated for wave periods $T = 1.0, 1.5, 2.0, 2.5$ s, and $d = 1.5$ m. The indicated periods and water depth were chosen to correspond with the periods and water depth used in experiments (discussed later).

Table 2
The standard deviation of the wave direction error estimates vs. # phase difference measurements (P) based on the polygonal array (Fig. 4(a)) with $D = 1.33$ m and $N = 4$. The particular sensor pairs considered in each simulation are indicated in the parentheses next to each number in the column P with (—"—) representing the sensor pairs in the above row. The standard deviations (deg) are computed from $100\times\sqrt{\hat{\mathbf{P}}_k(1,1)}$ at simulation time $t = 1000$ s, where $\hat{\mathbf{P}}_k(1,1)$ is the estimated error covariance of the UKF corresponding to the wave direction estimate. The multiplication factor of 100 is used to highlight the overall trend. For each wave direction, the UKF was applied to phase difference data generated by (9) with wave period $T = 2.0$ s and added Gaussian random noise with variances given by (18) and (20) with parameters $T_s = 0.1$ s and $\sigma = 1$ cm, respectively. The initial conditions and UKF parameters were identical for each run (see Table 1).

P	0°	30°	60°	90°	120°	150°	180°
2 : (1-2,1-3)	3.47	8.48	12.9	14.0	11.3	6.05	3.62
3 : (—"—,1-4)	3.41	4.62	5.17	4.65	3.42	2.67	3.43
4 : (—"—,2-3)	2.89	3.72	4.28	4.10	3.30	2.64	2.89
5 : (—"—,2-4)	2.58	2.67	2.77	2.85	2.79	2.59	2.58
6 : (—"—,3-4)	2.58	2.58	2.58	2.59	2.60	2.59	2.58

how the accuracy and covariance of the wave estimates change with the number of phase difference measurements. The simulation results (Table 2) indicate that the estimated error covariance decreases by increasing P, which corresponds to the number of independent phase difference measurements. The results also suggest that after a certain number of measurements, the improvement in the error variance is minimal. Hence, additional sensors may have benefits, but only up to a specific limit.

Furthermore, as P ($\leq P_{\max}(4) = 6$) increases, the estimated error covariances approach similar values on all wave directions, culminating in similarity at $P = 6$. It is worth emphasizing that this pattern is not general but a coincidence resulting from the geometry of the considered sensor array (Fig. 4a). Due to the symmetry of the sensors, the error covariance becomes progressively independent of the wave direction as $P \to 6$. This pattern is, in general, not duplicated for asymmetrical sensor arrays, which produce a greater spread of values.

4.4. Linear arrays

In general, the wave direction and wave number cannot be resolved uniquely from a linear shipboard configuration of two or more sensors. For instance, if a harmonic wave passes through two sensors at the same time, a zero phase difference will be detected and a third non-collinear sensor is needed to determine the direction. Without this third noncollinear sensor, there will be a 180° ambiguity in the direction since we do not know whether the wave is approaching from left or right. However, in the special case where information about the general wave direction is known beforehand (e.g., close to the shoreline such as in Hardisty (1988)), shipboard linear arrays may be used to find the wave direction (Fig. 8). As seen in Fig. 8, the wave direction can be determined from two sensors alone, provided that we know which side the waves are approaching. In this case, if the waves suddenly change direction to the other side (i.e., between 0 and $-\pi$), we get an ambiguity within a mirror symmetry (Fernandes et al., 1988, 2000). Also note that for linear arrays to work, the wave number should be known in advance.

5. Experimental verification

In this section, we give experimental verification of the UKF algorithm by applying it to experimental data from multiple shipboard IMUs. The raw IMU data needs to be processed through several steps such as data processing, choice of reference sensor, and wave frequency and phase difference estimation to ensure that the phase differences are

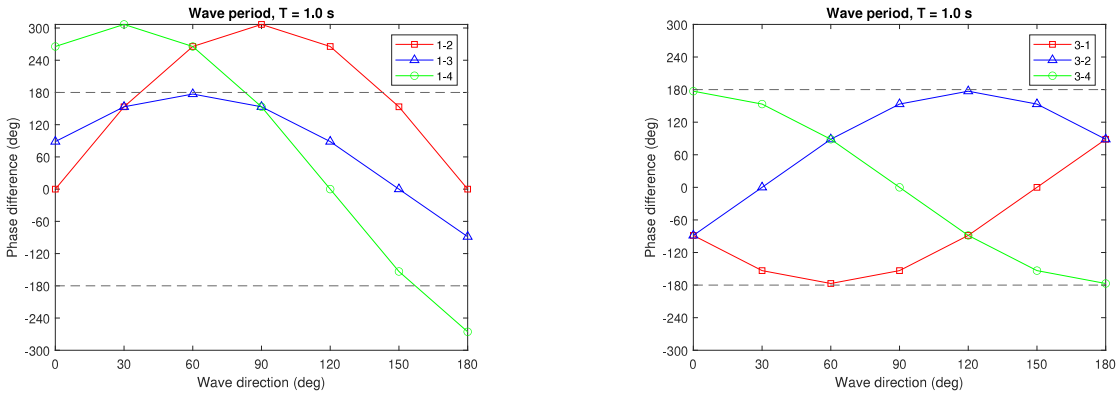

(a) Reference sensor = 1 (b) Reference sensor = 3

Fig. 6. The theoretical phase difference is plotted against the wave direction using (9) for two different choices of reference sensor in the polygonal array (Fig. 4a) with $D = 1.33$ m and $D' = 0.768$ m. For sensor pairs 1–2 and 1–4, several of the phase differences lie outside $(-\pi, \pi)$, whereas for sensor pairs 3-1, 3-2, and 3-4, all reside within $(-\pi, \pi)$.

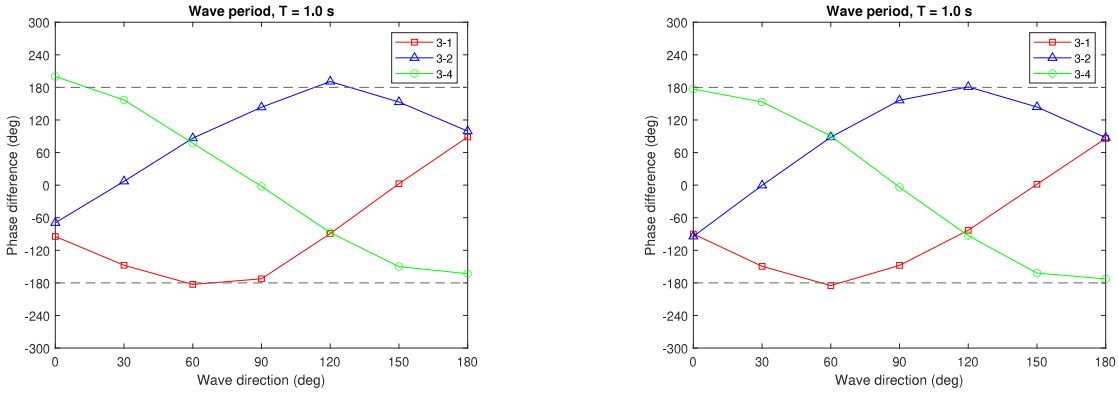

(a) $T_s = 0.1$ s (b) $\sigma = 1$ cm

Fig. 7. Gaussian random noise with variance given by (18) and (20) has been added separately to the phase differences in Fig. 6b. In (a) and (b) we can see how the sensor sampling time (T_s) and location error (σ), respectively, may cause some of the phase differences to become ambiguous.

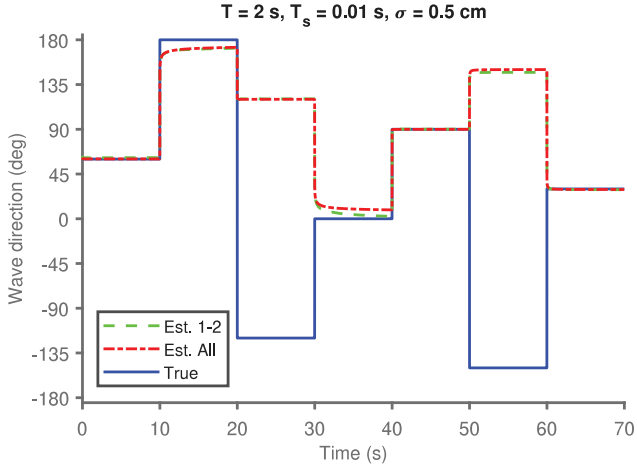

Fig. 8. Online estimates of the wave direction given by the UKF algorithm (Algorithm 1) with the linear array shown in Fig. 4b ($D = 0.5$ m). The phase differences were simulated using (9) with wave period $T = 2.0$ s and Gaussian random noise with variance given by (18) and (20) with $T_s = 0.01$ s and $\sigma = 0.5$ cm, respectively. The wave estimates are based on two sets of measurements (i.e., sensor pair 1–2 and all sensor pairs 1–2, 1–3, 1–4) with sensor 1 as reference. The wave number is assumed known.

obtained with as little error as possible. In the following subsections, we discuss each of these steps. The experimental data considered in this work was originally collected as part of the Master's thesis of Udjus (2017).

5.1. Experimental design

As explained in Udjus (2017), the authors equipped a 1:90 scaled model C/S Inocean Cat I Drillship (CSAD) (Fig. 9) with four spatially distributed ADIS16364 IMUs along the hull to record the vessel motions caused by waves. The IMU array configuration considered in the experiments is illustrated in Fig. 10. Each IMU is connected to an Arduino microprocesser, which is responsible for sampling the IMU data. The time synchronization of all four IMUs was handled by an interrupt signal from one (master) Arduino microprocessor to the other (slave) Arduinos. We refer to the Master's thesis of Udjus (2017) and references therein for additional details on the hardware and experimental design.

The experiments were carried out in the NTNU Marine Cybernetics laboratory, which contains a 1.5 m deep wave basin equipped with a wavemaker. The wavemaker is a 6-meter wide paddle operated by an electrical servo actuator and has a DHI wave synthesizer for producing regular and irregular waves.[2] The CSAD position and orientation was confined using ropes with 1 kg weights attached to each end (Fig. 9). This setup ensured that motions in surge, sway, and yaw were limited, while still allowing nearly free motions in heave, roll, and pitch.

A total of 52 regular wave experiments were carried out in the wave basin. For each relative wave direction {0°, 30°, 60°, 90°, 120°, 150°,

[2] For more details see: https://www.ntnu.edu/imt/lab/cybernetics.

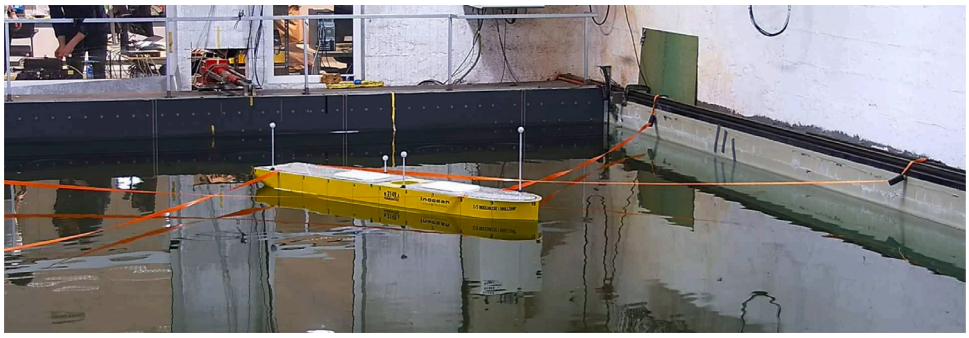

Fig. 9. The model ship C/S Inocean Cat I Drillship (CSAD) used in experiments. The position and orientation were held fixed by ropes with 1 kg weights attached to each end. Image reproduced with courtesy of Udjus (2017).

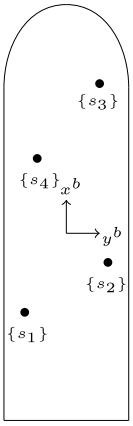

	x^b	y^b	z^b
s_1	-465	-184	-73
s_2	-244	184	-13
s_3	740	130	82
s_4	450	-160	82

Fig. 10. An illustration of the sensor configuration used in the wave experiments by Udjus (2017). IMUs 1, 2, 3, and 4 are denoted $\{s_1\}, \{s_2\}, \{s_3\}$, and $\{s_4\}$, respectively. The location of each sensor is given in millimeters with respect to the body-fixed reference frame $\{b\}$, which is defined midships with the z-axis pointing downwards (into the page).

180°}, regular waves with wave periods $\{1.0\text{ s}, 1.5\text{ s}, 2.0\text{ s}, 2.5\text{ s}\}$ lying within the frequency range of wind-generated surface gravity waves (Holthuijsen, 2007), were tested. A wave height of 5 cm was considered in all wave basin experiments, which, in reality, corresponds to a 4.5 m wave height (using Froude scaling with model scale 1:90). Although a 4.5 m wave height can be considered a very rough sea state (Price and Bishop, 1974), the roll and pitch responses in the experiments were small owing to the large vessel size.[3] According to the authors, the beach was not functioning as intended during the day of experimentation and, to avoid the impact of reflected waves, experiments were stopped after approximately 50 s, which, consequently, became the time duration of the recorded IMU data.

5.2. Data processing

In this section, we discuss some data processing steps needed to obtain an estimate of the vessel heave acceleration from the specific force measurements of each IMU. As we shall see, the heave accelerations are needed to compute the phase differences, which, in turn, will be used to estimate the desired wave quantities.

The accelerometers in an IMU measure the specific force $\mathbf{f}^a$ with respect to the inertial reference frame $\{i\}$. The readings are expressed in the accelerometer frame $\{a\}$, defined by the orientation of the accelerometer-sensitive axes. The $\{a\}$-frame may be non-orthogonal and misaligned and can be compensated via the rotation matrix $\mathbf{R}_a^s$, which converts raw measurements into the IMU sensor frame $\{s\}$ defined by the IMU manufacturer. The $\{s\}$-frame may suffer from installation errors caused by the alignment and inner distances of the sensor array. In order to align the $\{s\}$-frame with the body frame $\{b\}$, which is the referential frame used in the evaluation of the following heave acceleration, an additional rotation matrix $\mathbf{R}_s^b$ is required. The matrices $\mathbf{R}_a^s$ and $\mathbf{R}_s^b$ can be respectively obtained via the calibration procedures available at the site of the IMU manufacturer and after the IMUs have been installed into the array on the vessel. The sensor array positioning errors and their effects are discussed in Section 3.3.2.

For an ideal three-axis accelerometer, the specific force is given by

$$\mathbf{f}_{is}^b = \mathbf{a}_{is}^b - \mathbf{g}^b = \mathbf{R}_s^b \mathbf{R}_a^s \mathbf{f}^a,$$

where $\mathbf{a}_{is}^b$ is the linear acceleration of the IMU sensor frame $\{s\}$ with respect to the inertial frame $\{i\}$ expressed in $\{b\}$, and $\mathbf{g}^b$ is the gravity vector expressed in $\{b\}$. In practice, after treating the deterministic sensor imperfections discussed in Section 3.3.1, the measurements from a three-axis accelerometer are, in general, still subject to several stochastic errors. A common approach is to separate these errors and model them, respectively, as additive zero-mean Gaussian white noise and a drifting bias term. Following this approach, we can use the standard three-axis accelerometer sensor model from Fossen (2021), i.e.,

$$\mathbf{f}_{is}^b = \mathbf{a}_{is}^b - \mathbf{g}^b + \mathbf{b}_{\text{acc}}^b + \mathbf{w}_{\text{acc}}^b, \tag{24}$$

where $\mathbf{b}_{\text{acc}}^b$ and $\mathbf{w}_{\text{acc}}^b$ denote the respective bias and noise of the three-axis accelerometer. In general, (24) should be transformed to the navigational frame $\{n\}$ such that the linear *heave* acceleration from each sensor can be extracted and used to compute the phase differences. However, since we are only considering small roll and pitch angles, it is sufficient in this case to only consider the z-component of (24), i.e.,

$$f_{z,is}^b = a_{z,is}^b - g\cos\phi\cos\theta + b_{z,\text{acc}}^b + w_{z,\text{acc}}^b, \tag{25}$$

where ϕ and θ are the roll and pitch angles between $\{n\}$ and $\{b\}$, and g is the gravitational constant. In the following, we walk through the steps needed to obtain an estimate of the linear acceleration $a_{z,is}^b$, which corresponds to the heave acceleration when assuming small angles.

As explained in Udjus (2017), a separate camera-based tracking system called Qualisys was used to obtain measurements of the roll and pitch angles. These measurements showed that, in all experiments, ϕ and θ were less than 1° during the first 15 s and less than 2° for

[3] The model drillship corresponds to a 232 m × 40 m × 19 m vessel which are the standard dimensions of many drillships.

Table 3
The separation distance R_{ij} in meters between sensors $\{s_i\}$ and $\{s_j\}$ for the experimental configuration in Fig. 10.

		j			
	R_{ij}	1	2	3	4
i	1	-	0.4293	1.2452	0.9153
	2	0.4293	-	0.9855	0.7746
	3	1.2452	0.9855	-	0.4101
	4	0.9153	0.7746	0.4101	-

the remaining time of the experiments with wave excitation. Since $\cos(2°)^2 \approx 1$, (25) can be approximated by

$$f^b_{z,is} \approx a^b_{z,is} - g + b^b_{z,\text{acc}} + w^b_{z,\text{acc}}. \tag{26}$$

The initial bias in each accelerometer was estimated by computing the expected value of (26) and assuming that the accelerometers were level and at rest. Applying these assumptions to (26), yields

$$\begin{aligned}
\mathbb{E}\left[f^b_{z,is}\right] &= \mathbb{E}\left[a^b_{z,is} - g + b^b_{z,acc} + w^b_{z,acc}\right] \\
\mathbb{E}\left[f^b_{z,is}\right] &= \underbrace{\mathbb{E}\left[a^b_{z,is}\right]}_{=0} - g + b^b_{z,acc} + \underbrace{\mathbb{E}\left[w^b_{z,acc}\right]}_{=0} \\
b^b_{z,acc} &= \mathbb{E}\left[f^b_{z,is}\right] + g,
\end{aligned} \tag{27}$$

where $w^b_{z,acc}$ vanishes due to the Gaussian zero-mean assumption. Since the vessel only underwent wave excitation for 30–35 s, it is assumed that the initial sensor bias remained more or less constant throughout each experiment. This assumption is validated by the accelerometer Allan Variance curve found in the ADIS16364 datasheet, which states that for a 30 s time interval the in-run bias stability is around ± 0.1 mg.

The high-frequency noise components were removed by lowpass filtering the specific force measurements above the maximal wave frequency, resulting in the final estimated acceleration signal

$$\hat{a}^b_{z,is} = \bar{f}^b_{z,is} + g + \hat{b}^b_{z,\text{acc}}, \tag{28}$$

where $\bar{f}^b_{z,is}$ is the lowpass filtered specific force and $\hat{b}^b_{z,\text{acc}}$ is the initial bias estimate obtained through (27).

5.3. Choice of reference sensor

To resolve the wave direction and wave number associated with all the experimental wave periods $\{1.0\text{ s}, 1.5\text{ s}, 2.0\text{ s}, 2.5\text{ s}\}$, care must be exercised when selecting the reference sensor. As we shall see, the appropriate reference IMU can be chosen by examining the criterion (22) for each wave period and checking which IMU has all its neighboring separation lengths within the imposed limits. As discussed in Section 4.1, abidance to this criterion ensures that the theoretical phase differences are restricted to $(-\pi, \pi)$, thus avoiding spatial aliasing.

A comparison between the separation distances given by the experimental configuration (Table 3) and the separation limits imposed by Barber and Doyle (Fig. 5) reveals that only some of the IMUs can be used to resolve waves with period $T = 1.0$ s. In particular, we see that IMU 2 or 4 should be considered as a reference along with sensor pairs 2-1 and 2-4 or 4-2 and 4-3. With these choices, the Barber and Doyle criterion (22) is (in theory) satisfied for all experimental wave periods with the given IMU configuration.

5.4. Wave frequency and phase difference estimation

We have in the analysis thus far tacitly assumed the wave frequency ω to be perfectly known. The reliance on ω can be seen in the computation of the phase difference (16), the measurement covariance related to (18) and (20), and implicitly in the lowpass filtered acceleration signals (28). Hence, the wave frequency is an important cornerstone and requires accurate determination in order for our wave algorithm to function optimally.

For regular waves it is reasonable to assume that the vessel acceleration (28) can be modeled by a single sinusoid and perturbation of the form

$$\hat{a}^b_{z,is}(t) = A\sin(\omega t + \epsilon) + \delta(t), \tag{29}$$

where A, ω, ϵ, and δ represent the respective amplitude, frequency, phase, and perturbation of the acceleration signal pertaining to sensor $\{s\}$. Hence, the task at hand is to find an accurate estimate of ω from $\hat{a}^b_{z,is}$ assuming it can be modeled according to (29) with unknown parameters A, ω, ϵ, and bounded perturbation $\delta(t)$. In the following three subsections, we describe three different methods that can be used to achieve this goal.

5.4.1. Averaging the time intervals between successive peaks

A straightforward approach to finding the frequency of a sinusoid is to average the time intervals between the (detected) successive peaks of the signal. The averaged time intervals should be identical to the period given that the signal in question is a simple sinusoid. A prerequisite for this approach to work on signals of the form (29) is that the amplitude of the perturbation term δ is significantly smaller than the amplitude A. In other words, the signal (29) should have a sufficiently high signal-to-noise ratio (SNR). A high SNR will help prevent noisy spikes from being detected and confused as the actual signal peaks. In cases where the signal is significantly corrupted by noise, the SNR may be improved through various filtering techniques.

5.4.2. The Aranovskiy frequency estimator

The frequency identification algorithm of Aranovskiy et al. (2007) is designed based on a sinusoid of the form (29) and is attractive for two reasons. First, it offers a real-time implementation, rendering it suitable for many applications in need of quick frequency estimates where the measured signal can be approximated by a sinusoid. Second, it has shown robustness in the presence of unaccounted perturbations in the measurement signal.

The algorithm comprises an auxiliary filter and an adaptive observer of the form

$$\begin{aligned}
\dot{\xi}_1 &= \xi_2, \\
\dot{\xi}_2 &= -2\omega_f \xi_2 - \omega_f^2 \xi_1 + \omega_f^2 w(t), \\
\dot{\hat{\theta}} &= k\xi_1(\dot{\xi}_2 - \hat{\theta}\xi_1),
\end{aligned} \tag{30}$$

where $w(t) = \hat{a}^b_{z,is}(t)$ is the measured signal (here chosen as the estimated acceleration signal), ω_f is the user-specified filter cut-off frequency, $k > 0$ is the observer gain (not to be confused with the wave number), and $\theta := -\omega^2$. Both ω_f and k affect the convergence rate and steady state error of $\hat{\theta}$ to θ and should be selected based on the desired performance. In general, small ω_f and k will result in a slower convergence rate, whereas larger values will result in faster convergence but with some induced oscillation in steady-state (Belleter et al., 2015).

For marine craft operating in situations with little wave excitation, algorithm (30) can be modified to include an adaptive gain-switching mechanism for the observer gain k, as proposed by Belleter et al. (2015). This mechanism enables k to be switched between a high and a low gain depending on the amplitude of the measured roll, pitch, or heave responses, which may improve the convergence rate of the estimator. The reader is referred to Belleter et al. (2015) for additional theory and implementation details of the gain-switching mechanism.

5.4.3. The fast Fourier transform

In reality, ocean waves are usually irregular, exhibiting a broad spectrum of frequencies. In such situations, the time-averaging and Aranovskiy frequency estimator algorithms may be limited due to their inherent single-frequency model assumption. Unless the wave spectrum is sufficiently narrow, these approaches may struggle to identify the dominant (peak) frequency, which is the frequency component often

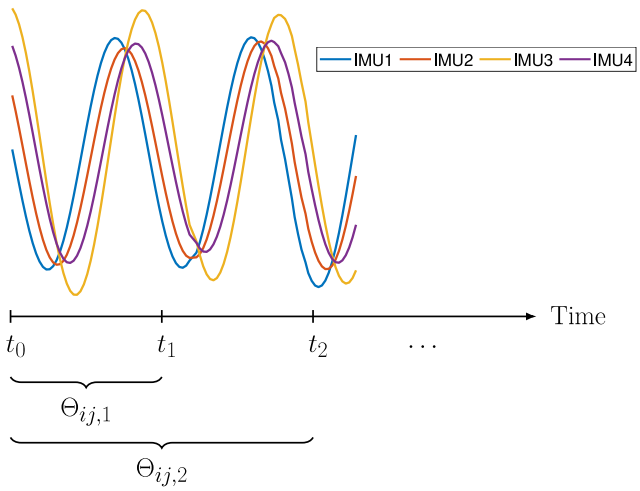

Fig. 11. The phase difference $\Theta_{ij,k}$ between IMUs $\{s_i\}$ and $\{s_j\}$ at time t_k can be estimated online by considering the linear heave acceleration signals within a window, before being passed on to the UKF. In this time window, the lag (i.e., the number of samples) between the respective heave signals is estimated by computing the cross-correlation between them and converting it to a phase difference using (16). The initial width of the window is set equal to the wave period and increases from t_0 as the signals continue to develop.

sought in marine applications. For a signal comprising multiple frequencies, the fast Fourier transform (FFT) can be used to deconstruct its spectral composition and identify any potential peaks. Unlike the above methods, the FFT does not make any assumptions on the structure or shape of the signals considered, thus making it a more viable option for analyzing signals comprising multiple frequencies. However, a drawback of this approach is that it cannot be implemented in real-time as it relies on back-dated information, which, as a consequence, produces a lag in the estimation.

Despite the attractive features of the Aranovskiy frequency estimator, the FFT was selected as the main method in this paper. This decision was based on two points: First, the FFT gave the most consistent frequency estimates for all experimental wave periods, in close agreement with the ground truth values, whereas the Aranovskiy estimator was somewhat less accurate and had difficulties identifying wave period $T = 1.0$ s (the reasons are discussed in Section 5.5.3). Second, as a proof of concept of Theorem 1 and in the compromise between accuracy and computational lag, we currently deem a higher accuracy in the wave estimates more important than real-time performance.

5.4.4. Phase difference estimation

After an estimate of the wave frequency has been obtained using either of the approaches described in Sections 5.4.1–5.4.3, the phase difference between the respective heave acceleration signals (28) can be estimated by computing the cross-correlation between them. This operation can be performed online by considering the heave acceleration signals within an increasing time window (Fig. 11).

5.5. Results and discussion

In this section, we present the results from our UKF wave algorithm on the experimental IMU data of Udjus (2017). The raw IMU data was processed according to the previous subsections to ensure that the phase differences could be obtained with as little error as possible and reduce the risk of ambiguities before being passed on to the UKF algorithm (Fig. 12). In the following results, the reference wave number was computed using the dispersion relation (21) with pool depth $d = 1.5$ m and the true wave period (i.e., the wave period used as input to the wavemaker machine). The reference wave direction was computed by fixing the boat heading (Fig. 9) and confirming this value with the Qualisys camera system.

5.5.1. Experimental verification of Theorem 1

The experimental results (Fig. 13) show that in 91% and 86% of experiments considered, the absolute wave direction and wave number errors based on three IMUs are less than 5° and 0.1 m^{-1}, respectively. These numbers provide strong evidence in favor of Theorem 1 and also validate the UKF capabilities in estimating those quantities. Experimental verification of Theorem 1 extends previous findings (Udjus, 2017; Heyn et al., 2017), which only seem to consider the wave direction, and not the wave number—although, as we have now shown, can also be determined simultaneously from the same data. Additionally, we have demonstrated that as few as three IMUs are in theory sufficient, provided that they are noncollinearly arranged and separated in accordance with (22).

The experimental results (Fig. 13) also show that in 71% and 52% of experiments considered, the measurement set $\{\Theta_{23}, \Theta_{24}\}$ (yellow) constitutes the largest error in each wave quantity, with some errors significantly exceeding the other sets of phases within each experiment. The large deviations observed can be linked to large errors in the estimated phase differences $\hat{\Theta}_{23}$ and $\hat{\Theta}_{24}$, which, in turn, are caused by several potential sources of error affecting IMUs $\{s_3\}$ and $\{s_4\}$. In general, the error between the estimated and actual phase differences can be attributed (either directly or indirectly) to one or more of the following sources: sensor imperfections, inexact sensor positioning and alignment, insufficient sensor sampling rate, shortcomings in the experimental design (e.g., from using ropes to confine boat heading and position), modeling errors due to small-angle approximation, wave frequency estimation, and oscillations and/or transient effects on the sensors due to structural vibrations and external environmental influences. From the above list, however, only inaccuracies in the sensor positioning and alignment of $\{s_3\}$ and $\{s_4\}$ may realistically explain the significant separation of errors within the sets of some experiments (we expect the errors caused by the other sources to manifest themselves roughly equally among the phase differences). As we have seen earlier, errors in the sensor locations can produce significant biases in the phase difference estimates (especially for short wave periods; see Fig. 3), which may translate to biases in the wave direction and wave number estimates. In order to test this theory, we have conducted a small simulation study investigating how the positioning errors of sensors $\{s_3\}$ and $\{s_4\}$ may impact the wave estimate errors associated with measurement sets $\{\Theta_{21}, \Theta_{23}\}$, $\{\Theta_{21}, \Theta_{24}\}$, and $\{\Theta_{23}, \Theta_{24}\}$. The results (Fig. 14) exhibit a similar error pattern to the results in Fig. 13, indicating that the location uncertainty of $\{s_3\}$ and $\{s_4\}$ is a plausible cause for the large separation of errors observed. This argument is further substantiated by Udjus (2017), which states that the sensor positions were obtained using a folding ruler and that some measurement errors may transpire because of this.

5.5.2. Multiple independent phase measurements

The experimental results also suggest that using additional independent phase measurements by adding more IMUs may reduce overall errors by having an "averaging" effect on the various measurement sets. Indeed, by studying the errors in Fig. 13 carefully, we see that the error obtained from the set of all six phase measurements is, in general, lower than the worst performing set constituting two phases. The reasons for this can be linked to the error variance, which is discussed in Section 4.3.

5.5.3. High-frequency waves

Contrary to wave periods $T = 1.5$ s, 2.0 s, and 2.5 s, obtaining accurate estimates of the wave direction and wave number proved difficult for the IMU data corresponding to $T = 1.0$ s (Fig. 15). The significant errors observed are caused by large errors in the estimated phase differences (Fig. 16), which, in turn, can be linked to several sources of error. In the following, we discuss some potential sources that we believe can have contributed to the deviations observed in Fig. 16.

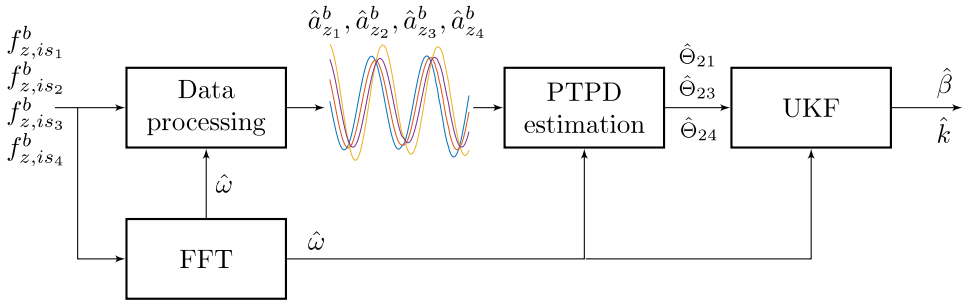

Fig. 12. A block diagram illustrating the general procedure of going from raw IMU measurements to obtaining estimates of the wave direction β and wave number k. The procedure can be summarized in three steps: (a) data processing, (b) PTPD estimation, and (c) state estimation. In (a) sensor biases and high-frequency (HF) noise are removed from the IMU measurements, yielding an estimate of the linear heave acceleration associated with each IMU (assuming small roll and pitch angles). The HF noise is filtered using a lowpass filter with cut-off above $\hat{\omega}$, obtained from a fast Fourier transform (FFT) applied to the entire data sequence. In (b) we estimate the phase difference $\hat{\Theta}$ online by following the procedure explained in Fig. 11. Finally, in (c) we apply the UKF algorithm to obtain the desired wave estimates.

A close look at some of the IMU data corresponding to $T = 1.0$ s (Fig. 17a) shows that the heave responses are non-sinusoidal, indicating that some distortion has taken place. This suspicion is confirmed by the corresponding FFTs of the data (Fig. 17b), which reveal additional frequencies in proximity to the expected single peak frequency. The existence of additional frequencies is a violation of the fundamental regularity/single-frequency assumption that our PTPD model is built on and may, as a result, be the reason for the poor estimation quality.

The distortion observed in Fig. 17a can most likely be attributed to the lowpass wave filtering characteristics of a ship (Nielsen, 2007, 2008; de Souza et al., 2018; Nielsen et al., 2019; Nielsen and Dietz, 2020), which occur whenever the waves are sufficiently short. For sufficiently short waves, multiple wave crests (and troughs) will affect the vessel simultaneously, resulting in a non-sinusoidal (filtered) response. This high-frequency filtering effect happens when the wavelength is shorter than the length of the wave trajectory through the vessel (i.e., the vessel length as seen by the waves). As seen in Fig. 18, the length of the wave trajectory depends on the orientation of the vessel relative to the waves, meaning that high-frequency filtering will not necessarily happen for all wave directions when considering waves of a given wavelength. It can be shown (see Appendix B) that the wave trajectory distance W through a box-shaped vessel along the wave propagation axis x^w (see Fig. 1 for definition) is

$$W = L|\cos\beta| + B|\sin\beta|, \tag{31}$$

where β is the relative wave direction, and L and B are the respective length and beam dimensions of the vessel. In order to avoid the high-frequency filtering effect, the wavelength λ should ideally be larger than W for a given β. This result can be generalized for all β if $\lambda > W$ for $\beta = \arctan(B/L)$ (see Appendix B for proof).

To quantitatively assess the potential occurrence of high-frequency filtering in our experiments, (31) was computed for all wave directions and compared to the wavelengths associated with each wave period (Fig. 19). In all the conducted experiments with $T = 1.0$ s ($\lambda = 1.5613$ m), except for $\beta = 90°$, W exceeds the wavelength, thus confirming the presence of high-frequency filtering in the vessel dynamics. Moreover, this result corresponds well with the observed estimation errors in Fig. 15, which shows significant errors for all wave directions except $\beta = 90°$.

The effect of high-frequency filtering is a known problem and, in general, a core limitation of wave estimation methods based on wave-induced vessel motions (Nielsen, 2007, 2008; de Souza et al., 2018; Nielsen et al., 2019; Nielsen and Dietz, 2020). Unfortunately, the problem can, as of now, only be alleviated by considering other responses that are less affected by filtering (Nielsen, 2008; de Souza et al., 2018). However, this requires additional complementary sensors not installed on the ship in the present study.

Phase ambiguities resulting from a precarious selection of sensor pairs represent another potential error source for wave period $T = 1.0$ s. As discussed in Section 5.3, only sensor pairs 2-1 and 2-4 will (in theory) satisfy the Barber and Doyle criterion (22), thus guaranteeing that phase differences Θ_{21} and Θ_{24} are within $(-\pi, \pi)$. This result can be seen from Fig. 16, which also shows that the theoretical phase difference Θ_{23} is outside $(-\pi, \pi)$ for wave directions $\{0°, 30°, 150°, 180°\}$, indicating that Θ_{23} should not be relied upon in the computation of those values. Nevertheless, the theoretical values of Θ_{23} were computed under the assumption that the sensor locations given in Fig. 10 are correct. However, as pointed out in Section 5.5.1, this is not necessarily true, meaning that the actual Θ_{23} may be within the range of $(-\pi, \pi)$ for several wave directions. In particular, we suspect that this may be the case for wave directions $\{0°, 30°, 150°\}$, since the estimated phases remain somewhat close to the theoretical values and should ideally have been wrapped to angles of opposite sign.

Table 4
The sum of wave direction $\tilde{\beta}$ and wave number $\tilde{k}$ errors corresponding to "All" phases in Figs. 13 and 15 for each respective wave period T. The total errors $\tilde{\beta}$ and $\tilde{k}$ are given in degrees and m^{-1}, respectively. Notice that the total errors decrease as the wave period gets longer and vice versa.

T	$\tilde{\beta}$	$\tilde{k}$
1.0	366.23	27.12
1.5	74.05	0.95
2.0	44.80	0.62
2.5	41.74	0.56

Recall from the analysis of Section 3.3.2 that inexact sensor positions produce a bias in the computed phase difference that grows exponentially as the wave period becomes smaller (Fig. 3). This effect may be one of the reasons for the overall growth of errors observed in the wave estimates when comparing them with the respective wave periods (Table 4). The bias caused by the sensor positioning may also render some of the phase differences ambiguous by "pushing" them outside the range $(-\pi, \pi)$, as discussed in Section 4.2. Studying Fig. 16 closely, it is possible that this may have occurred for Θ_{24} at wave directions $\{120°, 150°, 180°\}$ since the angles below the boundary $-\pi$ wrap to values in proximity to the estimates of Θ_{24}.

5.5.4. Future work

Today, most shipboard wave estimation methods are based on response amplitude operators (RAOs) that are capable of producing estimates of the complete directional wave spectrum (Waals et al., 2002; Tannuri et al., 2003; Pascoal and Guedes Soares, 2009; Brodtkorb et al., 2018). These methods differ from our approach, which is signal-based (i.e., it requires no ship information) and built on regular harmonic waves, thus limiting it to information about the main (dominant) wave direction and wave number. It is currently unknown how well this method will work for more irregular wave patterns comprising many frequencies and directions. Hence, future investigations will aim at

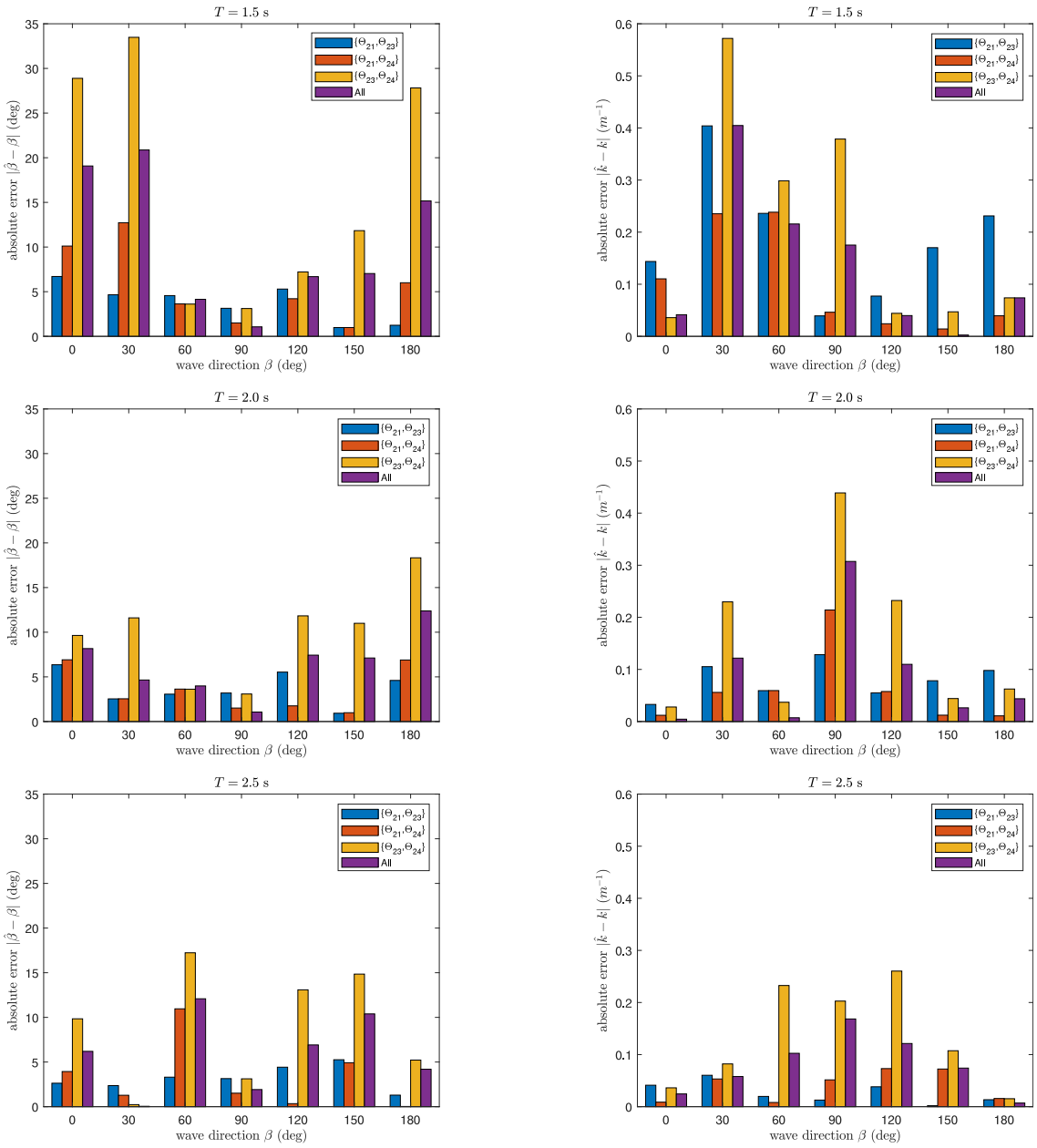

Fig. 13. Results from wave experiments with wave periods $T = 1.5$ s, 2.0 s, 2.5 s, and sampling time $T_s = 0.01$ s (100 Hz). The various sets of phase difference measurements are $\{\Theta_{21}, \Theta_{23}\}$, $\{\Theta_{21}, \Theta_{24}\}$, $\{\Theta_{23}, \Theta_{24}\}$, $\{\Theta_{12}, \Theta_{13}, \Theta_{14}, \Theta_{23}, \Theta_{24}, \Theta_{34}\}$ (all) corresponding to IMUs $\{s_1, s_2, s_3\}$, $\{s_1, s_2, s_4\}$, $\{s_2, s_3, s_4\}$, $\{s_1, s_2, s_3, s_4\}$, respectively, and are shown with different colors. For each set of IMUs, the bar plots show the absolute error between the wave estimates (after convergence) and the true values. (For interpretation of the references to color in this figure legend, the reader is referred to the web version of this article.)

experimental testing of the UKF in such wave environments, with the possibility of extending the algorithm to utilize the complete phase model (4) with roll-pitch compensation such that the UKF may be applied to all vessels in both moderate and higher sea states.

The transition from geographically fixed wave arrays to portable shipboard wave arrays has increased the practical usefulness of the PTPD approach. As a next research step, the possibility of using the PTPD approach for moving vessels with a non-zero forward speed shall be investigated. In order to accommodate this capability, the forward vessel speed should be considered in the PTPD model derivation, which generally causes frequency shifts in the measured vessel motions due to the Doppler effect. Hence, future work will also target wave direction estimation for underway vessels by extending our PTPD approach to consider the shifted wave (encounter) frequency.

6. Conclusions

This paper has added several extensions to the existing literature on shipboard and traditional wave arrays considering the phase-time-path-difference (PTPD) concept. We have shown (through observability analysis and experimental data) that *both* the wave direction and wave number can be obtained from a minimum of three noncollinear sensors (e.g., IMUs) measuring regular harmonic waves, assuming a dynamically positioned surface vessel with small roll and pitch angles. In this regard, we proposed a signal-based unscented Kalman filter (UKF) algorithm to estimate these wave quantities, which offers several benefits over the standard analytical solution (7) in terms of addressing uncertainties and incorporating multiple measurements. We have discussed and quantified several sources of error related to the sensors (e.g., sensor imperfections, insufficient sampling rate, and oscillations

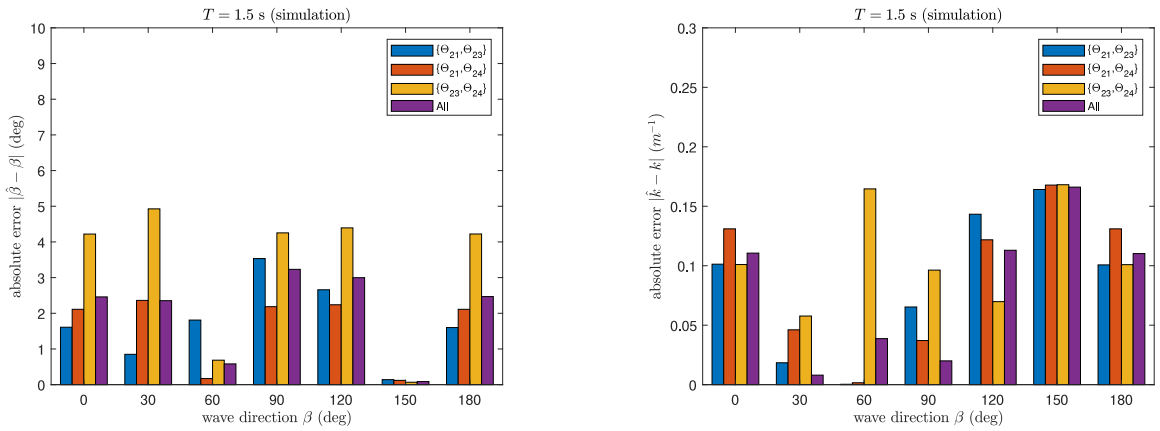

Fig. 14. Results from simulation with sensor positioning errors. The various sets of phase difference measurements are $\{\Theta_{21}, \Theta_{23}\}$, $\{\Theta_{21}, \Theta_{24}\}$, $\{\Theta_{23}, \Theta_{24}\}$, $\{\Theta_{21}, \Theta_{23}, \Theta_{24}\}$ (all) corresponding to IMUs $\{s_1, s_2, s_3\}$, $\{s_1, s_2, s_4\}$, $\{s_2, s_3, s_4\}$, $\{s_1, s_2, s_3, s_4\}$, respectively, and are shown with different colors. For each set of IMUs, the bar plots show the absolute error between the wave estimates (after convergence) and the true values. The respective phase differences $\{\Theta_{21}, \Theta_{23}, \Theta_{24}\}$ were simulated using (9) with $T = 1.5$ s, sampling time $T_s = 0.01$ s, and adding positioning errors to all sensors (configured according to Fig. 10). The errors were added as Gaussian random noise to the configuration matrix of (10) with variance given by (20) using $\sigma_{21} = 2$ cm, $\sigma_{23} = 10$ cm, and $\sigma_{24} = 10$ cm. (For interpretation of the references to color in this figure legend, the reader is referred to the web version of this article.)

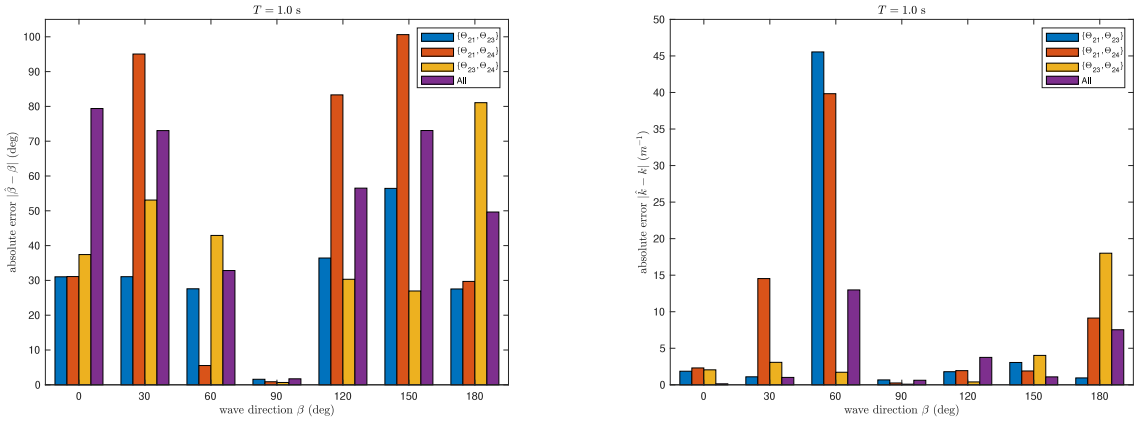

Fig. 15. Results from wave experiments with wave period $T = 1.0$ s and sampling time $T_s = 0.01$ s (100 Hz). The various sets of phase difference measurements are $\{\Theta_{21}, \Theta_{23}\}$, $\{\Theta_{21}, \Theta_{24}\}$, $\{\Theta_{23}, \Theta_{24}\}$, $\{\Theta_{12}, \Theta_{13}, \Theta_{14}, \Theta_{23}, \Theta_{24}, \Theta_{34}\}$ (all) corresponding to IMUs $\{s_1, s_2, s_3\}$, $\{s_1, s_2, s_4\}$, $\{s_2, s_3, s_4\}$, $\{s_1, s_2, s_3, s_4\}$, respectively, and are shown with different colors. For each set of IMUs, the bar plots show the absolute error between the wave estimates (after convergence) and the true values. (For interpretation of the references to color in this figure legend, the reader is referred to the web version of this article.)

and transient effects) and array construction (e.g., inexact sensor locations) and shown how some of these errors can be incorporated into the UKF to yield the estimated uncertainty in the wave estimates. Finally, we have shown how the Barber and Doyle criterion (22), together with some of the errors above, should be considered in the design of shipboard wave arrays.

Our proposed PTPD model and UKF algorithm hinge on regular harmonic waves, meaning that the practicality of this approach is currently restricted to ocean waves resembling such wave patterns (e.g., narrow-banded wave trains such as swell). It is presently unknown how well the UKF will work in more complex sea environments. Future study will aim at experimental testing of the UKF in such environments, with the possibility of extending the algorithm to estimate vessel roll and pitch motions, thus enabling the complete phase model (4) to be used instead. Such an extension will render the UKF algorithm appropriate to *any* surface vessel in moderate *and* higher sea states. Future work will also target wave direction estimation for underway vessels by extending our PTPD approach to consider the wave encounter frequency.

CRediT authorship contribution statement

Johann A. Dirdal: Conceptualization, Methodology, Software, Investigation, Formal analysis, Writing, Visualization. **Roger Skjetne:** Conceptualization, Writing – review & editing. **Jan Roháč:** Conceptualization, Writing – review & editing. **Thor I. Fossen:** Conceptualization, Writing – review & editing, Supervision.

Declaration of competing interest

The authors declare that they have no known competing financial interests or personal relationships that could have appeared to influence the work reported in this paper.

Acknowledgments

The work was sponsored by the Research Council of Norway (RCN) through the Centre of Excellence on Autonomous Marine Operations and Systems (NTNU AMOS, RCN project 223254), and partly through the Centre for Research-based Innovation, SFI MOVE (RCN project 237929). The research was also partially funded by the ESIF, EU Operational Programme Research, Development and Education, and from the Center of Advanced Aerospace Technology (CZ.02.1.01/0.0/0.0/16 019/0000826) carried out at the Faculty of Mechanical Engineering, Czech Technical University in Prague.

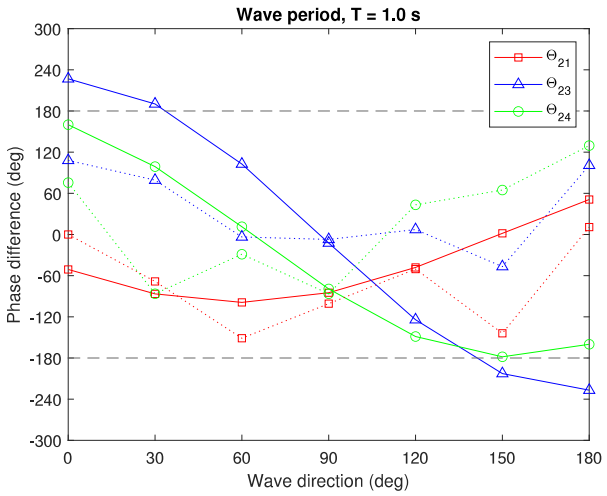

Fig. 16. The theoretical (solid) vs. estimated (dotted) phase differences $\{\Theta_{21}, \Theta_{23}, \Theta_{24}\}$ for wave period $T = 1.0$ s and sensor configuration given by Fig. 10 using $\{s_2\}$ as reference. The theoretical values were computed using (9), whereas the corresponding estimates were calculated from cross-correlations (Fig. 11) between the processed IMU data for $T = 1.0$ s.

Appendix A. Observability analysis

In this appendix, we show that the relative wave direction β and wave number k of a harmonic wave can be uniquely determined from a minimum of three noncollinear sensors, given a dynamically positioned surface vessel with small roll and pitch angles. In the following analysis, we consider two separate cases: wave number k known and wave number k unknown. As we shall see, the minimum sensor requirements stated in Theorem 1 apply in both cases. Theorem 1 shall be proven by showing that the nonlinear state–space model (10) is (locally) observable for a minimum of two phase difference measurements, which corresponds to three sensors. The forthcoming observability analysis hinges on the definitions of nonlinear observability (Nijmeijer, 1990; Marino and Tomei, 1996), which are stated below for convenience.

Definition 1. The system

$$\begin{aligned} \dot{\mathbf{x}} &= \mathbf{f}(\mathbf{x}), \quad \mathbf{x} \in \mathbb{R}^n, \\ \mathbf{z} &= \mathbf{h}(\mathbf{x}), \end{aligned} \tag{A.1}$$

is said to be locally observable in U_0, a neighborhood of the origin, if

$$\operatorname{rank}\{d\mathbf{h}, \dots, d(L_{\mathbf{f}}^{n-1}\mathbf{h})\} = n, \quad \forall \mathbf{x} \in U_0, \tag{A.2}$$

If (A.2) holds for every $\mathbf{x} \in \mathbb{R}^n$ we say that the system is observable.

Definition 2. The observation space $\mathbb{O}$ of the system (A.1) is the linear space (over $\mathbb{R}^n$)

$$\mathbb{O} = \operatorname{span}\{L_{\mathbf{f}}^{n-1} h_i\}, \quad i = 1, \dots, p.$$

The observability codistribution is given by the observation space by

$$d\mathbf{h} = \operatorname{span}\{d\mathbf{H}(\mathbf{x}) \ : \ \mathbf{H} \in \mathbb{O}\},$$

where

$$d\mathbf{H} = \frac{\partial \mathbf{H}}{\partial x_1} dx_1 + \frac{\partial \mathbf{H}}{\partial x_2} dx_2 + \cdots + \frac{\partial \mathbf{H}}{\partial x_n} dx_n.$$

Case A: Wave number known

Sensors $N = 2$

If we assume the wave number to be a known quantity, then the state–space model in (10) can be reduced to the following scalar system

$$\begin{aligned} \dot{x} &= 0, \\ z &= h(x) = k \begin{bmatrix} R_{12}\cos\alpha_{12} & R_{12}\sin\alpha_{12} \end{bmatrix} \begin{bmatrix} \cos x \\ \sin x \end{bmatrix}, \end{aligned} \tag{A.3}$$

where $z = \Theta_{12}$ and $x = \beta \in (-\pi, \pi]$. The measurement equation can be expanded and written more compactly as

$$z = k R_{12} \cos(x - \alpha_{12}),$$

which, for a single phase difference $z = \Theta_{12}$ (two sensors), has two solutions given by $\pm(x - \alpha_{12})$. Hence, (A.3) is not observable from a single pair of sensors.

Sensors $N = 3$

Adding an additional sensor, (A.3) now becomes

$$\begin{aligned} \dot{x} &= 0, \\ \mathbf{z} = \mathbf{h}(x) &= \begin{bmatrix} R_{12}\cos\alpha_{12} & R_{12}\sin\alpha_{12} \\ R_{13}\cos\alpha_{13} & R_{13}\sin\alpha_{13} \end{bmatrix} \begin{bmatrix} \cos x \\ \sin x \end{bmatrix}, \end{aligned} \tag{A.4}$$

where $\mathbf{z} = [\Theta_{12}, \ \Theta_{13}]^\top$ and $x = \beta \in (-\pi, \pi]$. The system above can be condensed by defining constants a_1, a_2, b_1, b_2 such that

$$\mathbf{h}(x) = \begin{bmatrix} h_1 \\ h_2 \end{bmatrix} = \begin{bmatrix} a_1 & b_1 \\ a_2 & b_2 \end{bmatrix} \begin{bmatrix} \cos x \\ \sin x \end{bmatrix} = \begin{bmatrix} a_1\cos x + b_1 \sin x \\ a_2 \cos x + b_2 \sin x \end{bmatrix}.$$

The observation space $\mathbb{O}$ (Definition 2) of (A.4) is determined by computing the Lie derivatives up to $n = 1$, i.e.,

$$L_f^0 \mathbf{h} = [h_1, \ h_2]^\top,$$

which yields the observation space

$$\begin{aligned} \mathbb{O} &= \operatorname{span}\{h_1, h_2\} \\ &= \operatorname{span}\{a_1 \cos x + b_1 \sin x, a_2 \cos x + b_2 \sin x\}. \end{aligned}$$

Using this result, the observability codistribution can be formed as

$$\begin{aligned} d\mathbf{H} = \frac{\partial \mathbf{h}}{\partial x} dx &= \begin{bmatrix} \frac{\partial h_1}{\partial x} & \frac{\partial h_2}{\partial x} \end{bmatrix}^\top dx \\ &= \begin{bmatrix} -a_1 \sin x + b_1 \cos x \\ -a_2 \sin x + b_2 \cos x \end{bmatrix} dx \\ &= \begin{bmatrix} -a_1 & b_1 \\ -a_2 & b_2 \end{bmatrix} \begin{bmatrix} \sin x \\ \cos x \end{bmatrix} dx, \end{aligned}$$

and, finally, we get

$$\begin{aligned} d\mathbf{h} &= \operatorname{span}\{d\mathbf{H}\} \\ &= \operatorname{span}\left\{ \begin{bmatrix} -a_1 & b_1 \\ -a_2 & b_2 \end{bmatrix} \begin{bmatrix} \sin x \\ \cos x \end{bmatrix} dx \right\}. \end{aligned}$$

The observability codistribution $d\mathbf{h}$ will have full rank as long as the above coefficient matrix is non-singular. This condition can easily be checked by evaluating when the determinant is zero, i.e.,

$$\det\left(\begin{bmatrix} -a_1 & b_1 \\ -a_2 & b_2 \end{bmatrix} \right) = -a_1 b_2 + b_1 a_2 = 0.$$

Inserting the expressions for a_1, a_2, b_1, b_2 into the above expression and simplifying it, yields

$$k^2 R_{12} R_{13} \sin(\alpha_{12} - \alpha_{13}) = 0.$$

Since $k, R_{12}, R_{13} > 0$, the above expression is zero only when the sensors lie on the same line, i.e., $\alpha_{12} = \alpha_{13}$. Hence, for $N = 3$ (three sensors) we have from Definition 1 that

$$\operatorname{rank}\{d\mathbf{h}\} = 1 = n \quad \forall x \in (-\pi, \pi] \subseteq \mathbb{R},$$

as long as the sensors are arranged in a noncollinear configuration. Since x is only defined between $(-\pi, \pi]$, which is a subset of $\mathbb{R}$, the system (A.4) is by definition *locally* observable.

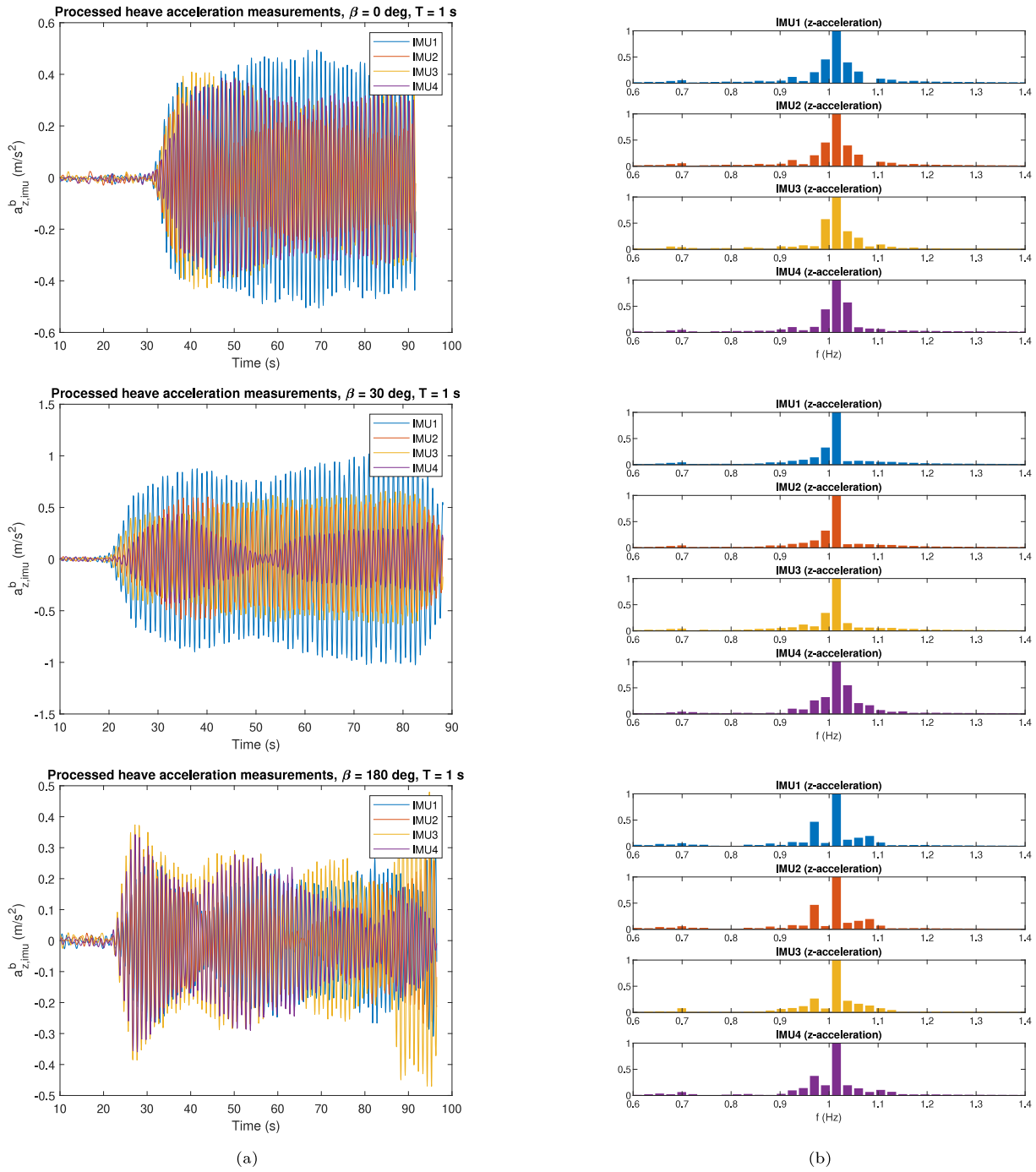

(a) (b)

Fig. 17. (a) Heave accelerations (after processing) for wave experiments with period $T = 1.0$ s and wave directions $\{0°, 30°, 180°\}$, and (b) the corresponding FFTs. The FFTs were normalized by dividing all values in each respective plot by the corresponding maximum. The peak wave frequency in all the FFTs is located at $f = 1.015$ Hz, which corresponds to a wave period $T = 0.985$ s.

Case B: Wave number unknown

Sensors $N = 2$

If we assume the wave number to be an unknown quantity, then the state–space model in (10) reduces to

$$\dot{\mathbf{x}} = \mathbf{0},$$
$$z = h(\mathbf{x}) = \begin{bmatrix} R_{12}\cos\alpha_{12} & R_{12}\sin\alpha_{12} \end{bmatrix} \begin{bmatrix} x_2\cos x_1 \\ x_2 \sin x_1 \end{bmatrix}, \tag{A.5}$$

where $z = \Theta_{12}$, $\mathbf{x} = [x_1,\ x_2]^\top = [\beta,\ k]^\top$, and $x_1 \in (-\pi, \pi]$ and $x_2 \in \mathbb{R}^+$. The measurement equation can be expanded and written more compactly as

$$z = R_{12}x_2\cos(x_1 - \alpha_{12}),$$

which, for a single phase difference $z = \Theta_{12}$ (two sensors), has multiple solutions. Hence, the system (A.5) is not observable from a single pair of sensors.

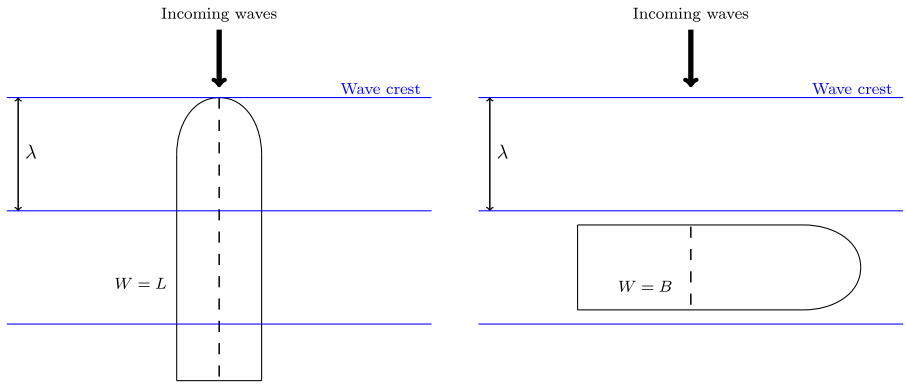

Fig. 18. The length of the wave trajectory W (represented by dashed lines) depends on the relative wave direction β. When $\beta = 180°$ (left), the vessel will filter the waves (shown in blue) passing through it as the wavelength $\lambda < W = L$, where L is the vessel length. However, when $\beta = 90°$ (right), the vessel motion responses will be unaffected by filtering as $\lambda > W = B$, where B is the vessel beam.

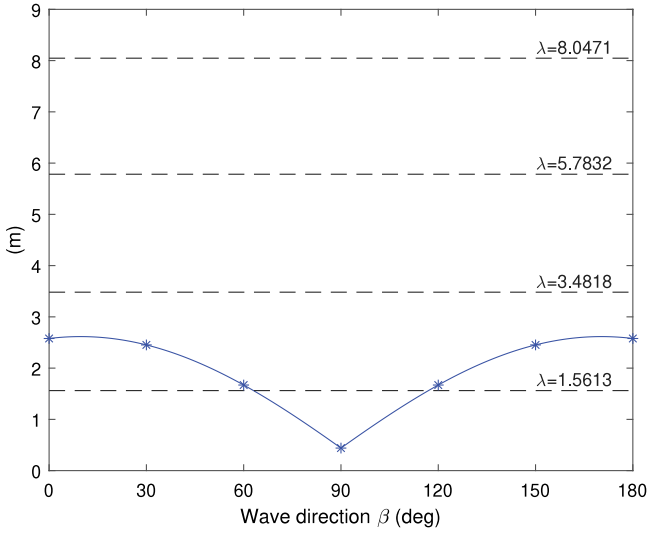

Fig. 19. The wave trajectory distance W (solid blue line) computed from (31) vs. experimental wavelengths λ (dashed lines). The value of W associated with each experimental wave direction β is indicated with an asterisk. The length and beam dimensions of the model ship used in the experiments are $L = 2.58$ m and $B = 0.44$ m, respectively. For each wave period $T = 1.0$ s, 1.5 s, 2.0 s, and 2.5 s, the corresponding wavelength $\lambda = 2\pi/k$ is computed using (21) with $d = 1.5$ m.

Sensors $N = 3$

Adding an additional sensor, (A.5) now becomes

$$\dot{\mathbf{x}} = \mathbf{0},$$
$$\mathbf{z} = \mathbf{h}(\mathbf{x}) = \begin{bmatrix} R_{12}\cos\alpha_{12} & R_{12}\sin\alpha_{12} \\ R_{13}\cos\alpha_{13} & R_{13}\sin\alpha_{13} \end{bmatrix} \begin{bmatrix} x_2\cos x_1 \\ x_2\sin x_1 \end{bmatrix}, \tag{A.6}$$

where $\mathbf{z} = [\Theta_{12},\ \Theta_{13}]^\top$, $\mathbf{x} = [x_1,\ x_2]^\top = [\beta,\ k]^\top$, and $x_1 \in (-\pi, \pi]$ and $x_2 \in \mathbb{R}^+$. The system above can be condensed by defining constants a_1, a_2, b_1, b_2 such that

$$\mathbf{h}(\mathbf{x}) = \begin{bmatrix} h_1 \\ h_2 \end{bmatrix} = \begin{bmatrix} a_1 & b_1 \\ a_2 & b_2 \end{bmatrix} \begin{bmatrix} x_2\cos x_1 \\ x_2\sin x_1 \end{bmatrix} = \begin{bmatrix} a_1x_2\cos x_1 + b_1x_2\sin x_1 \\ a_2x_2\cos x_1 + b_2x_2\sin x_1 \end{bmatrix}.$$

The observation space $\mathbb{O}$ (Definition 2) of (A.6) is then determined by computing the Lie derivatives up to $n = 2$, i.e.,

$$L_{\mathbf{f}}^0\mathbf{h} = [h_1,\ h_2]^\top,$$
$$L_{\mathbf{f}}^1\mathbf{h} = \frac{\partial \mathbf{h}}{\partial \mathbf{x}}\mathbf{f} = \mathbf{0}, \quad \text{since } \mathbf{f}(\mathbf{x}) = \mathbf{0},$$

which yields the observation space

$$\mathbb{O} = \text{span}\{h_1, h_2\}$$
$$= \text{span}\{a_1x_2\cos x_1 + b_1x_2\sin x_1, a_2x_2\cos x_1 + b_2x_2\sin x_1\}.$$

Using this result, the observability codistribution can be formed as

$$d\mathbf{H} = \frac{\partial \mathbf{h}}{\partial x_1}dx_1 + \frac{\partial \mathbf{h}}{\partial x_2}dx_2 = \underbrace{\begin{bmatrix} \frac{\partial h_1}{\partial x_1} & \frac{\partial h_1}{\partial x_2} \\ \frac{\partial h_2}{\partial x_1} & \frac{\partial h_2}{\partial x_2} \end{bmatrix}}_{\partial \mathbf{h}/\partial \mathbf{x}} \begin{bmatrix} dx_1 \\ dx_2 \end{bmatrix}$$
$$= \begin{bmatrix} -a_1x_2\sin x_1 + b_1x_2\cos x_1 & a_1\cos x_1 + b_1\sin x_1 \\ -a_2x_2\sin x_1 + b_2x_2\cos x_1 & a_2\cos x_1 + b_2\sin x_1 \end{bmatrix} \begin{bmatrix} dx_1 \\ dx_2 \end{bmatrix},$$

with

$$d\mathbf{h} = \text{span}\{d\mathbf{H}\}.$$

The observability codistribution $d\mathbf{h}$ will have full rank as long as the Jacobian $\partial\mathbf{h}/\partial\mathbf{x}$ is non-singular. This condition can easily be checked by evaluating the determinant, i.e.,

$$\det\left(\begin{bmatrix} -a_1x_2\sin x_1 + b_1x_2\cos x_1 & a_1\cos x_1 + b_1\sin x_1 \\ -a_2x_2\sin x_1 + b_2x_2\cos x_1 & a_2\cos x_1 + b_2\sin x_1 \end{bmatrix}\right)$$
$$= (-a_1x_2\sin x_1 + b_1x_2\cos x_1)(a_2\cos x_1 + b_2\sin x_1)$$
$$- (a_1\cos x_1 + b_1\sin x_1)(-a_2x_2\sin x_1 + b_2x_2\cos x_1)$$
$$= -a_1b_2x_2(\sin^2 x_1 + \cos^2 x_1)$$
$$+ b_1a_2x_2(\sin^2 x_1 + \cos^2 x_1)$$
$$= x_2(-a_1b_2 + b_1a_2).$$

Inserting the expressions for a_1, a_2, b_1, b_2 into the equation above, simplifying, and equating it to zero, yields

$$x_2R_{12}R_{13}\sin(\alpha_{12} - \alpha_{13}) = 0.$$

Since $x_2, R_{12}, R_{13} > 0$, the above expression is zero only when the sensors lie on the same line, i.e., $\alpha_{12} = \alpha_{13}$. Hence, for $N = 3$ (three sensors), we have from Definition 1 that

$$\text{rank}\{d\mathbf{h}\} = 2 = n \quad \forall x_1 \in (-\pi, \pi],\ \forall x_2 \in \mathbb{R}^+,$$

as long as the sensors are arranged in a noncollinear configuration. Since x_1 and x_2 are only defined in $(-\pi, \pi]$ and $\mathbb{R}^+$, respectively, which are both subsets of $\mathbb{R}$, the system in (A.6) is by definition *locally* observable.

Appendix B. Finding an expression of the wave trajectory distance

In this appendix, we derive an analytical expression of the wave trajectory distance through the vessel (i.e., the vessel length as seen by the waves) for a box-shaped vessel. With this expression, we can quantitatively assess when high-frequency filtering due to the vessel is likely to influence the measured motion responses for different wave periods and wave directions.

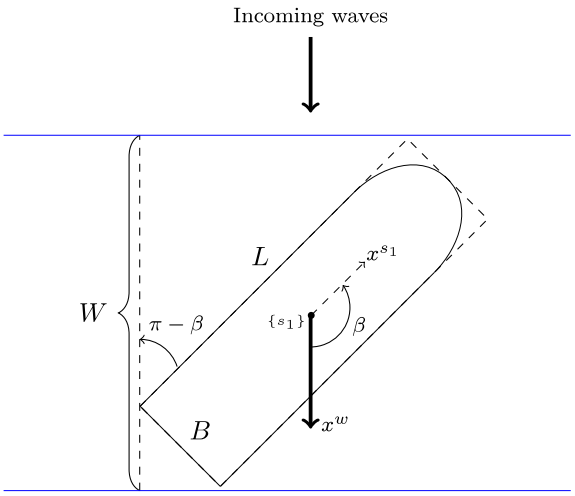

Fig. B.20. A vessel with length L and beam B dimensions measured at the waterline, oriented at an angle β relative to the incoming harmonic waves (wave crests shown in blue). The vessel hull has been approximated with a rectangle of length L and width B to simplify analysis. The definitions of the wave direction β, the tangent wave frame $\{w\}$ with wave propagation axis x^w, and reference sensor $\{s_1\}$ with sensor axis x^{s_1} are given in Fig. 1. The wave trajectory distance W is the distance the wave should travel across the vessel (i.e., the total distance in which the wave is in contact with the vessel).

Consider a vessel with length L and beam B measured at the waterline, oriented at an angle β relative to the incoming harmonic waves, as shown in Fig. B.20. In general, the first point on the vessel that the wave will affect is the corner closest to the initial wave, whereas the final exit point will be the diagonally-opposite corner. Using rudimentary trigonometric identities, the distance between these points along the wave propagation axis x^w can be expressed as

$$W = L|\cos\beta| + B|\sin\beta|, \tag{B.1}$$

where W is the wave trajectory distance and β is the relative wave direction. The maximum wave trajectory distance can be determined by taking the derivative of (B.1) with respect to β, which yields the following expression

$$\frac{dW}{d\beta} = L\left(\frac{-\cos\beta\sin\beta}{|\cos\beta|}\right) + B\left(\frac{\cos\beta\sin\beta}{|\sin\beta|}\right) = 0$$
$$\Rightarrow |\tan\beta| = \frac{B}{L},$$

and has four possible solutions

$$\beta = \pm\arctan(B/L) \text{ and } \beta = \pi \pm \arctan(B/L). \tag{B.2}$$

When the vessel is oriented at each of these wave directions, two of the corners will be furthest apart along the axis x^w. Hence, the wavelength λ should ideally be greater than W when β is given by (B.2) to avoid high-frequency filtering for all wave directions in the recorded motion responses.

References

Aranovskiy, S.V., Bobtsov, A.A., Kremlev, A.S., Luk'yanova, G.V., 2007. A robust algorithm for identification of the frequency of a sinusoidal signal. J. Comput. Syst. Sci. Int. 46 (3).

Barber, N., Doyle, D., 1956. A method of recording the direction of travel of ocean swell. Deep Sea Res. (1953) 3 (3).

Belleter, D.J., Galeazzi, R., Fossen, T.I., 2015. Experimental verification of a global exponential stable nonlinear wave encounter frequency estimator. Ocean Eng. 97.

Brodtkorb, A.H., Nielsen, U.D., Sørensen, A.J., 2018. Sea state estimation using vessel response in dynamic positioning. Appl. Ocean Res. 70.

Brown, R.G., Hwang, P.Y.C., 1997. Introduction to Random Signals and Applied Kalman Filtering: With MATLAB Exercises and Solutions, third ed. Wiley, New York, NY, URL: https://cds.cern.ch/record/680442.

de Souza, F.L., Tannuri, E.A., de Mello, P.C., Franzini, G., Mas-Soler, J., Simos, A.N., 2018. Bayesian estimation of directional wave-spectrum using vessel motions and wave-probes: Proposal and preliminary experimental validation. J. Offshore Mech. Arctic Engi. 140 (4).

Donelan, M.A., Drennan, W.M., Magnusson, A.K., 1996. Nonstationary analysis of the directional properties of propagating waves. J. Phys. Oceanogr. 26 (9).

Draycott, S., Davey, T., Ingram, D.M., Day, J.L.a., Johanning, L., 2015. Using a phase-time-path-difference approach to measure directional wave spectra in FloWave. In: EWTEC Conference Proceedings. pp. 1–7.

Draycott, S., Davey, T., Ingram, D.M., Day, A., Johanning, L., 2016. The SPAIR method: Isolating incident and reflected directional wave spectra in multidirectional wave basins. Coast. Eng. 114, 265–283.

Draycott, S., Noble, D.R., Davey, T., Bruce, T., Ingram, D.M., Johanning, L., Smith, H.C., Day, A., Kaklis, P., 2018. Re-creation of site-specific multi-directional waves with non-collinear current. Ocean Eng. 152.

Duz, B., Mak, B., Hageman, R., Grasso, N., 2019. Real time estimation of local wave characteristics from ship motions using artificial neural networks. In: 14th Int. Conf. of Practical Design of Ships and Other Floating Structures. Yokohama, Japan.

Esteva, D.C., 1976. Wave direction computations with three gage arrays. In: Proc. Fifteenth Coastal Engng. Conf., (Hawaii Univ., U.S.A.: Jul. 11-17, 1976), Vol. 1, New Yo. p. 349–367.

Esteva, D.C., 1977. Evaluation of the computation of wave direction with three-gauge arrays. Technical report, Technical Paper No. 77-7, CERC, U.S. Army Corps of Engineers.

Fernandes, A.A., Gouveia, A.D., Nagarajan, R., 1988. Determination of wave direction from linear and polygonal arrays. Ocean Eng. 15 (4), 345–357.

Fernandes, A.A., Menon, H.B., Sarma, Y.V., Jog, P.D., Almeida, A.M., 2001. Wavelength of ocean waves and surf beat at Duck from array measurements. In: Proceedings of the International Symposium on Ocean Wave Measurement and Analysis, Vol. 2.

Fernandes, A.A., Sarma, Y.V., Menon, H.B., 2000. Directional spectrum of ocean waves from array measurements using phase/time/path difference methods. Ocean Eng. 27 (4), 345–363.

Fossen, T.I., 2021. Handbook of Marine Craft Hydrodynamics and Motion Control, second ed. Wiley, Chichester, West Sussex, U.K..

Fu, T.C., Fullerton, A.M., Hackett, E.E., Merrill, C., 2011. Shipboard measurement of ocean waves. In: Proceedings of the International Conference on Offshore Mechanics and Arctic Engineering - OMAE, Vol. 6.

Hardisty, J., 1988. Measurement of shallow water wave direction for longshore sediment transport. Geo-Mar. Lett. 8 (1).

Haseltine, E.L., Rawlings, J.B., 2005. Critical evaluation of extended Kalman filtering and moving-horizon estimation. Ind. Eng. Chem. Res. 44 (8).

Heyn, H.M., Udjus, G., Skjetne, R., 2017. Distributed motion sensing on ships. In: OCEANS 2017 - Anchorage, Vol. 2017-January.

Holthuijsen, L.H., 2007. Waves in Oceanic and Coastal Waters. Cambridge University Press.

Julier, S., Uhlmann, J., 2004. Unscented filtering and nonlinear estimation. Proc. IEEE 92 (3).

Kandepu, R., Imsland, L., Foss, B.A., 2008. Constrained state estimation using the unscented Kalman filter. In: 2008 Mediterranean Conference on Control and Automation - Conference Proceedings, MED'08.

Luo, L., Liu, S., Li, J., Jia, W., 2020. Deterministic reconstruction and reproduction of multi-directional irregular waves based on linear summation model. Ocean Eng. 198, 106952.

Mak, B., Düz, B., 2019. Ship as a wave buoy: Using simulated data to train neural networks for real time estimation of relative wave direction. In: Proceedings of the International Conference on Offshore Mechanics and Arctic Engineering - OMAE, Vol. 9.

Marino, R., Tomei, P., 1996. Nonlinear Control Design: Geometric, Adaptive and Robust. Prentice Hall International (UK) Ltd, GBR.

Nielsen, U.D., 2006. Estimations of on-site directional wave spectra from measured ship responses. Mar. Struct. 19 (1).

Nielsen, U.D., 2007. Response-based estimation of sea state parameters - influence of filtering. Ocean Eng. 34 (13).

Nielsen, U.D., 2008. The wave buoy analogy - estimating high-frequency wave excitations. Appl. Ocean Res. 30 (2).

Nielsen, U.D., 2017. A concise account of techniques available for shipboard sea state estimation. Ocean Eng. 129.

Nielsen, U.D., Brodtkorb, A.H., Sørensen, A.J., 2019. Sea state estimation using multiple ships simultaneously as sailing wave buoys. Appl. Ocean Res. 83.

Nielsen, U.D., Dietz, J., 2020. Estimation of sea state parameters by the wave buoy analogy with comparisons to third generation spectral wave models. Ocean Eng. 216.

Nijmeijer, H., 1990. Nonlinear Dynamical Control Systems. Springer New York, New York, NY.

Pascal, R., Bryden, I., 2011. Directional spectrum methods for deterministic waves. Ocean Eng. 38 (13).

Pascal, R., Lucas, J., Ingram, D., Bryden, I., 2009. Assessing and improving the Edinburgh curved wave tank. In: Proceedings of the International Offshore and Polar Engineering Conference.

Pascoal, R., Guedes Soares, C., 2009. Kalman filtering of vessel motions for ocean wave directional spectrum estimation. Ocean Eng. 36 (6–7).

Price, W., Bishop, R., 1974. Probabilistic Theory of Ship Dynamics. Chapman and Hall, London.

Simon, D., 2010. Kalman filtering with state constraints: A survey of linear and nonlinear algorithms. IET Control Theory Appl. 4 (8).

Tannuri, E.A., Sparano, J.V., Simos, A.N., Da Cruz, J.J., 2003. Estimating directional wave spectrum based on stationary ship motion measurements. Appl. Ocean Res. 25 (5).

Udjus, G., 2017. Force Field Identification and Positioning Control of an Autonomous Vessel Using Inertial Measurement Units (MSc Thesis). Norwegian University of Science and Technology, Trondheim, p. 85.

Waals, O.J., Aalbers, A.B., Pinkster, J.A., 2002. Maximum likelihood method as a means to estimate the directional wave spectrum and the mean wave drift force on a dynamically positioned vessel. In: Proceedings of the International Conference on Offshore Mechanics and Arctic Engineering - OMAE, Vol. 4.